



Global WaterPack – A 250 m resolution dataset revealing the daily dynamics of global inland water bodies



Igor Klein ^{*}, Ursula Gessner, Andreas J. Dietz, Claudia Kuenzer

German Remote Sensing Data Center (DFD), German Aerospace Center (DLR), Oberpfaffenhofen, 82234 Wessling, Germany

ARTICLE INFO

Article history:

Received 17 December 2016

Received in revised form 24 June 2017

Accepted 29 June 2017

Available online 2 July 2017

Keywords:

Global surface water variability

Daily time resolution

MODIS

Cloud and gap free

ABSTRACT

Knowledge about inland surface water distribution and its short- to long-term variability is of high importance. Recently many studies have presented interesting results at regional, continental and global scale with 14.25 m to 25 km spatial and 10 day to one year temporal resolution. However, surface inland water bodies can feature temporally rapid spatial changes caused by extreme events, seasonal variability as well as human activity. Such changes can occur on temporal scales which are below the currently existing dynamic water body products. While the daily temporal resolution of available sensors has not been exploited yet. In this study we present an approach which uses the full temporal resolution of the Moderate Resolution Imaging Spectroradiometer (MODIS) to generate a 250 m daily global dataset of inland water bodies based on spectral information and dynamic thresholding. Based on a combination of MODIS Terra and Aqua daily classifications, auxiliary mask layers and temporal interpolation, a global cloud and gap free time series of inland water bodies is produced. The presented results are validated with 321 Landsat images across the globe. The executed validation shows an overall accuracy of 96.3% with 7.8% omission and 0.5% commission error, and a kappa coefficient of 93.3% for pure water pixels. The presented results demonstrate the high potential for different applications requiring information of inland water body dynamics at high temporal resolution. Examples demonstrate that e.g. the filling and emptying of water reservoirs, changes and inundation cycles of natural water bodies as well as freezing and thawing of lakes can be analyzed at a highly detailed temporal scale.

© 2017 Elsevier Inc. All rights reserved.

1. Introduction

The distribution of fresh water, its quality and amount are key factors for life on earth. Inland surface water bodies such as lakes, reservoirs, and rivers cover approximately 3% of the global land mass. They constitute essential terrestrial ecosystems, and play a crucial role in the global hydrological cycle, e.g. for water supply, agricultural production and hydropower generation (Feng et al., 2015; Palmer et al., 2015). Many inland water bodies are highly dynamic regarding their areal extent both at seasonal and inter-annual time scales. These temporally dynamic water bodies provide a wide range of ecosystem functions for the environment, they are nesting places for birds (Dodman and Diagana, 2006; Haas et al., 2009), maintain biodiversity of diverse specialized plants and animals (Zedler, 2003), and are of high cultural and socio-economic value (Hein, 2006). The Ramsar Convention on Wetlands has raised concerns about important wetland ecosystems because these decrease and their natural water regimes are altered noticeably worldwide e.g. due to use of fresh water for irrigation or regional environmental and climate variability (Gardner et al., 2015). On the other

side, several thousands of new artificial water bodies have been created e.g. for hydropower generation or as reservoirs for irrigation water causing a relocation of surface water resources (Pekel et al., 2016).

Detailed knowledge on inland water bodies' distribution, its annual and seasonal variability and long-term alterations can serve as an important source of information for water and ecosystem management (Cole et al., 2007), and political decision makers (Feyisa et al., 2014; Giardino et al., 2010) and is required in scientific research of various disciplines (e.g. Hydrology, Climate Modelling, Ecosystem Assessment). Water bodies can furthermore serve as a proxy for different variable and human activities. Particularly surface water in endorheic basins which instantaneously changes due to precipitation, snow melt and human upstream regulation (Mason et al., 1994). During the past decades, remote sensing has enabled large-area and multi-temporal analyses of the land surface, and powerful methods and tools have been developed for analyzing Earth observation data. Also for detecting the temporal and spatial variability of inland water bodies, remote sensing offers unique and valuable opportunities (Feng et al., 2014; Haas et al., 2009; Kuenzer et al., 2015, 2013; Ogilvie et al., 2015). Several studies focus on water detection from optical remote sensing data (Feyisa et al., 2014; Ji et al., 2009; Li et al., 2013; Sun et al., 2012). Optical sensors featuring medium spatial resolution such as the Moderate Resolution

^{*} Corresponding author.

E-mail address: igor.klein@dlr.de (I. Klein).

Imaging Spectroradiometer (MODIS), Visible Infrared Imaging Radiometer Suite (VIIRS), Ocean and Land Colour Instrument (OLCI) or Advanced Very-High-Resolution Radiometer (AVHRR) have the advantage of global coverage with daily resolution. The characteristics of water to strongly absorb at visible, near infrared (NIR), and short infrared (SWIR) wavelengths are well detectable by these optical sensors. The spectral features of water have been utilized for classification either through single band slicing of the NIR band (Jain et al., 2005; Klein et al., 2014), the difference index (NIR-RED) (Sun et al., 2011) or of spectral indices such as, the Normalized Difference Vegetation Index (NDVI) or the Normalized Difference Water Index (NDWI) (Boschetti et al., 2014; Gao, 1996; McFEETERS, 1996; Xu, 2006). Furthermore, an approach based on Hue-Saturation-Value (HSV) space has been applied to MODIS and Landsat data at continental and global scale (Pekel et al., 2016, 2014).

It has to be considered that inland water bodies feature different spectral characteristics over time and space (Feng et al., 2012; Fichtelmann and Borg, 2012; Liu, 2012). This can be caused e.g. by variations in water depth, bottom material, sediment load, chlorophyll content, dissolved organic carbon, aquatic vegetation, algae, turbidity and any combination of these variables and components. Additionally, in cold regions surface water can be covered by lake ice and snow. Furthermore, the detected spectral response is affected by changing atmospheric conditions, sun angle, and sensor view angle which complicates water classification (Liu, 2012; Ticehurst et al., 2014). Additional challenges arise through similar spectral characteristics of water and other land surfaces (e.g. volcanic materials, coal mines, burned areas), as well as shadows induced by e.g. clouds, relief and buildings. Established water mapping approaches have therefore used auxiliary datasets to identify and avoid related misclassifications (Copernicus GMES Initial Operations, 2013; Feng et al., 2015; Fichtelmann and Borg, 2012; Pekel et al., 2016). In addition to optical systems, there are active and passive radar sensors that are suited for water mapping, and provide the advantage of being cloud insensitive (Martinis et al., 2015; Papa et al., 2010). However, they feature either very coarse spatial resolution (microwave e.g. AMSR-E, SSM/I), longer revisit times and narrow geographical extent (e.g. Terra-SAR-X, RADARSAT-2), or cover shorter time periods (Sentinel-1, ASAR).

To date, several static global datasets exist that provide information on the spatial extent of water bodies and wetlands. The Global Lakes and Wetlands Dataset (GLWD) based on several Earth observation and national inventory data introduced by Lehner and Döll (2004) features a spatial resolution of 30 arc-seconds (approx. 1 km). The Shuttle Radar Topography Mission (SRTM) water body data (SWBD) is available for latitudes between 56°S and 60°N at 90 m resolution (Slater et al., 2006). The global 250 m MODIS water mask presented by Carroll et al. (2009) is a combination of MODIS data and SWBD. Recently, Verpoorter et al. (2014) introduced a static Global Water Bodies (GLOWABO) map with 14.25 m spatial resolution based on Landsat data from 2000 ± 3 years. Feng et al. (2015) presented their first version of a static global 30 m resolution inland water body map for ca-2000 derived from Landsat. Fluet-Chouinard et al. (2014) presented a global baseline map of mean annual minimum, mean annual maximum and long-term maximum inundation area at 500 m spatial resolution. Even though static water maps are adequate for some applications there is an increasing demand for information on the spatio-temporal variability of inland water bodies and their long-term evolution. Open Earth observation data archives provide time series which enable to generate such datasets. Many authors have already presented first comprehensive results in mapping water body dynamics at regional to continental scale (Feng et al., 2012; Fichtelmann and Borg, 2012; Haas et al., 2009; Klein et al., 2014; Mueller et al., 2016; Pekel et al., 2014; Tulbure et al., 2016). These datasets provide information on water body extents in temporal intervals of ten days to one month and cover limited geographic regions. Recently, Pekel et al. (2016) introduced an unprecedented dataset of global water surface maps based on Landsat 5, 7 and

8 data between 1984 and 2015 revealing changes of surface water on monthly time scale. Additionally, there are global near-real-time (NRT) flood services such as the NASA/DFO NRT Global Flood Mapping Product (Nigro et al., 2014), the Joint Research Center's (JRC) Global Integrated Flood Map (Groeve et al., 2013) or the multi-scale flood monitoring system based on MODIS and TerraSAR-X data (Martinis et al., 2013). These products focus on rapid flood monitoring and near-real-time services. These studies and products document large scale changes of surface inland waters around the globe. Because there are manifold reasons and drivers of observed variabilities, the changes can occur either gradually over longer time periods or abruptly within few days. Especially, rapid changes cannot be captured at high temporal detail or might be missed by monthly composites or static annual averages (Guerschman et al., 2011; Pekel et al., 2016; Yamazaki and Trigg, 2016).

Despite recent valuable achievements, a temporally-dense, daily cloud and gap free global dataset on water bodies' dynamics is not available yet. The necessity of such datasets however has been confirmed by the recent Global Climate Observing System (GCOS) report (WMO, 2016) which states that Essential Climate Variables (ECV) data records need to be established for water extent and lake ice cover ideally with daily temporal resolution and at 20 m and 300 m respectively. Temporally-dense and gap free information on inland surface water will open new perspectives for investigations on changing environment, climate and human activities. In this context, a long, multi-annual time series of daily water body extents will not only enhance our understanding of rapid changes after heavy rainfalls, snowmelt, or human water extraction and dam regulations. It will likewise allow to scientifically investigating gradual, long-term shifts in seasonal cycles of water bodies, such as subtle changes in the timing and duration of water extents that gradually develop several years. The daily representation of open water can furthermore contribute to an improved calibration, assimilation and validation of climate and hydrological models with high temporal resolution. This paper presents an approach which allows the global delineation of daily inland open surface water body extents at a spatial resolution of 250 m. As lake ice is not classified as open water surfaces, periods during which surface waters are covered by ice can be inferred. The interference of open water as no water because it is ice covered can only occur in climates where ice can form on open surface waters. The approach exploits the bi-diurnal spectral information recorded by the MODIS sensors on board of the satellites Terra and Aqua. The methodology consists of two main components. The first component classifies water pixels based on daily spectral information of the NIR and red channels using dynamic thresholding over time and space. These dynamic thresholds are established from a reference dataset. In the second component, the resulting daily water masks are further analyzed to remove cloud and data gaps. The presented approach builds on prior developments of Klein et al. (2015) with considerable improvements regarding input data, spatio-temporally dynamic thresholding and consistent time series generation. The presented results are a global product (Global WaterPack) of daily inland surface water extent, which allows an interpretation and better understanding of the temporal variability of natural and artificial water bodies. The method was developed and tested based on Terra and Aqua data from 2014. In this article we report mainly on results of this year, whereas the processing of the remaining entire Terra/Aqua archive is currently ongoing. Results were validated with total of 321 Landsat images across the globe and cross-compared with selected floods in 2014 as detected in NRT flood service. Selected examples of lakes, reservoirs and wetlands demonstrate the application potential of this novel dataset to contribute to a better understanding of water body dynamics and their interconnection with different driving forces.

2. Data

In this section all used input datasets as well as auxiliary data products are introduced. In Section 2.1 the main input datasets with diurnal

temporal resolution are explained. [Section 2.2](#) focuses on auxiliary datasets which are used for different mask generation required for post-classification. [Section 2.3](#) introduces all datasets which were acquired for training and validation processes. The key information and purpose of all input datasets are summarized in [Table 1](#).

2.1. Daily MODIS data

The main input datasets for this study are daily surface reflectances detected by the MODIS instruments aboard of Aqua and Terra. MODIS provides daily global coverage which is particularly useful for continental to global scale assessments. We used the MODIS surface reflectance products MOD09GQ/MYD09GQ (collection version 5, L2G) containing the NIR channel (841–876 nm) and the red channel (620–670 nm) at a spatial resolution of 250 m. Terra based datasets (MOD) are available since February 2000, whereas Aqua based datasets (MYD) are available since July 2002. The MOD09GQ/MYD09GQ datasets are level-2 gridded products and are provided as calibrated spectral radiance values estimating surface spectral reflectance at ground level (LP DAAC, 2015). Although the data went through atmospheric correction, atmospheric influences might in some cases not be fully eliminated but only minimized. Furthermore, the datasets feature some patchiness around water bodies and negative values above water due to overcorrection of atmospheric effects. Secondly, we used the MODIS daily snow cover level-3 products MOD10A1/MYD10A1 with a spatial resolution of 500 m (collection version 5, L3G). The thematic snow product provides daily information on snow cover, cloud cover, and lake ice as well as a static lake and ocean mask (Hall and Riggs, 2007; Riggs et al., 2006). Both datasets are provided as tiles (approx. 1200×1200 km) in Sinusoidal projection. The main global land mass excluding the pole regions and remote islands are covered by 206 tiles which results in more than 300,000 input datasets and data volume of about 15 terabytes for one calendar year (e.g. for a none leap year: 365 days * 2 sensors (Aqua and Terra) * 2 products (MxD09GQ and MxD10A1) * 206 tiles).

2.2. Datasets for post-classification

Recent studies on water detection based on optical sensors stated that there are multiple sources for commission errors which can be addressed by involving different masks derived from auxiliary data (Feng et al., 2015; Pekel et al., 2016; Yamazaki et al., 2015). We discriminate between two general sources for commission errors: geographical local sources which occur more or less permanently at the same location (e.g. topographic and building shadows, spectrally similar or land surfaces that are spectrally similar to water such as volcanic material), and spatially dynamic sources (e.g. cloud shadows and burned areas).

To target the permanent sources, the following additional information layers are used and later combined to a dynamically applicable

final mask ([Section 3.2.2](#)). A global digital elevation model (DEM) is required for the reduction of commission errors caused by relief shadows. A global DEM mainly based on SRTM 90 m digital elevation data was downloaded from CGIAR Consortium for Spatial Information. This DEM has been processed to fill data gaps in SRTM using different auxiliary DEM sources and is provided with 90 m spatial resolution in $5 \times 5^\circ$ tiles in a Geographic projection (Jarvis et al., 2008). Furthermore, shadows induced by buildings occur in urban areas. To identify dense urban structures, the urban class of the MODIS classification product MCD12Q1 was utilized (Friedl et al., 2010). Due to similar spectral characteristics overestimation of water can occur on land surfaces such as basalt fields, volcanic ashes, dark soils, open surface coal mines or surfaces covered by rock encrusting lichens. In order to reduce these misclassifications, we utilized the annual cycle parameters (ACP) from an annual land surface temperature product provided by Bechtel (2015), and the spectral information of the MOD09A1/MYD09A1 products as an additional dataset ([Section 3.2.2](#)). The value-added ACP dataset provides gap free information about land surface temperature and is based on MODIS land surface temperature measurements.

Finally, to target dynamic sources of commission errors, burned area information contained in the MODIS thermal anomalies and fire dataset MCD45A1 was used as a dynamic mask to minimize such commission errors. The reduction of cloud shadow influences is finally targeted within the temporal interpolation step which is discussed in [Section 3.3.4](#).

2.3. Data for dynamic threshold definition and validation

Landsat-8 images were used for the definition of dynamic thresholds and for validation. Landsat data have been utilized in many remote sensing studies as a proxy for ground truth to assess the accuracy of moderate resolution results (Carroll et al., 2009; Dietz et al., 2014; Gessner et al., 2015; Kuenzer et al., 2015; Pekel et al., 2016, 2014). In this study a total number of 321 Landsat scenes for 78 Landsat tile IDs were downloaded and processed ([Fig. 1](#)). For reasons of global representativeness, the Landsat tiles were spatially distributed over 13 different biomes defined by Olson et al. (2001).

The 13 biomes are summarized into four clusters regarding major climatological zones, vegetation types, similar water characteristics and major water classification challenges within these areas: polar and boreal biomes (PB) including Taiga and Tundra; arid and semi-arid biomes (ASE) including savannas and grasslands; and tropical and sub-tropical biomes (TST) including sub-tropical to tropical forests; temperate biomes (TE) including temperate forests. Open surface water within the PB cluster features pronounced freezing and thawing cycles, and low sun angles during the winter season complicate water classification. These effects lead to particular characteristics of the detected water body signal throughout the year. In the ASE cluster, cloud effects

Table 1
Input and reference datasets for the GWP.

Data code	Data name	Temporal resolution	Spatial resolution	Purpose
MOD09GQ MYD09GQ	Surface spectral reflectance	Daily	250 m	NIR & red band for water detection
MOD10A1 MYD10A1	Snow cover	Daily	500 m	Exclusion of clouded, snow covered, ice covered and ocean pixels from training
MOD44W	Water mask	Static	250 m	Selection of training pixel candidates
DEM	Digital elevation model	Static	90 m	Identification of relief shadows
MCD12Q1	Urban areas	Static	500 m	Identification of building shadows
ACP	Annual land surface temperature	Time-series	1000 m	Identification of ambiguous land surfaces e.g. volcanic ashes, basalt
MOD09A1 MYD09A1	Surface spectral reflectance	8-Day composites	500 m	Identification of ambiguous land surfaces e.g. volcanic ashes, basalt
MCD45A1	Thermal anomalies and fire	Monthly composites	1000 m	Identification of burned areas
LANDSAT 2D MWP	Surface spectral reflectance	~8 days	30 m	Dynamic threshold definition and validation
	MODIS water product	2-Day composite	250 m	Comparison of results

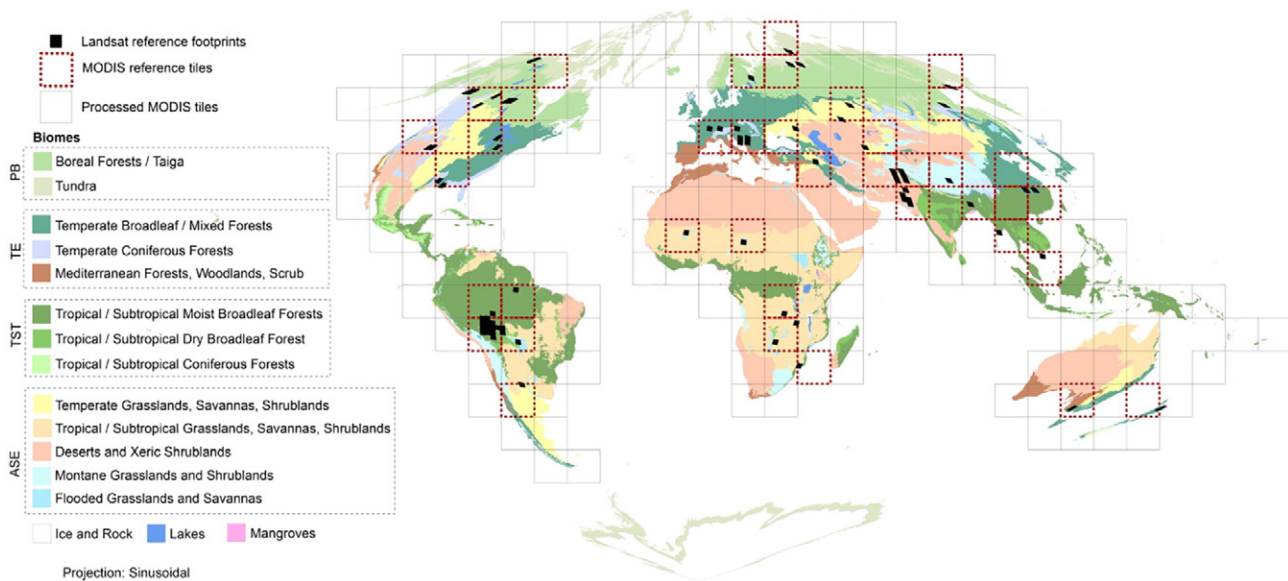


Fig. 1. Global distribution of Landsat footprints and corresponding MODIS tiles used for dynamic threshold definition and validation (PB = polar and boreal, TST = tropical and sub-tropical forests, TE = temperate, ASE = arid and semi-arid).

are comparably low whereas fires are frequent and burn scars are a major dynamic misclassification source. Additionally, the water bodies in this cluster can feature pronounced areal variations due to precipitation variability. Within the TST cluster, high cloud coverage is the major challenge. Furthermore, this cluster contains dense evergreen tree vegetation, and the data is acquired during constantly high sun elevation. The TE cluster is under the combined influence of most mentioned factors such as low sun angle and high cloudiness, burned areas and freezing and thawing cycles.

The distribution of the number of reference Landsat tiles (18 tiles for PB, 12 for TE, 12 tiles for TST, and 36 tiles for ASE) approximately follows the areal size of the four cluster: PB (~31 Mio km²), TE (~20 Mio km²), ASE (~64 Mio km²), TST (~22 Mio km²). The selection of Landsat tiles was purposive with the aim to cover the described challenges within each cluster.

For each Landsat tile ID multi-temporal scenes for the year 2014 (cloud cover less than 20%) were acquired. A higher number of multi-temporal datasets was chosen for areas with high surface water variability, in order to cover different open water extents as well as different environmental conditions and external influences. Thereafter, 35 scenes for PB, 40 scenes for TE, 76 scenes for TST, and 170 scenes for ASE represent the final sampling dataset. In addition to the reference datasets of Landsat, we acquired the 2-day composites of the MODIS Water Product (2D MWP) at 250 m spatial resolution from the experimental NASA/ DFO NRT Global Flood Mapping (Nigro et al., 2014). Three different flood events in 2014 were selected to compare the Global WaterPack (GWP) with 2D MWP.

As a basis for the identification of training pixel candidates and the subsequent dynamic threshold definition, the MODIS raster water mask at 250 m spatial resolution (Carroll et al., 2009) was utilized. This static dataset was produced from 16-day composites of MODIS 250 m reflectance data (Terra archive 2000–2008; Aqua archive 2002–2008) in combination with SWBD.

3. Methodology

3.1. Overview

The spectral characteristics of water to absorb light at near infrared and short infrared wavelengths is often exploited to delineate between water and land (Jain et al., 2006; Sun et al., 2012). However, inland

water bodies and their spectral characteristics vary in time and space, e.g. due to water depth variations, bottom material, sediment load, chlorophyll content, dissolved organic carbon, aquatic vegetation, algae, turbidity and coverage by ice and snow (Fichtelmann and Borg, 2012; Guerschman et al., 2011; Liu, 2012; Yamazaki et al., 2015). The absorption of water with different constituents is defined as the sum of the components' absorption (Gege, 2004). Additionally, VIS/NIR wavelengths can be affected by atmospheric conditions, sun angle and sensor view angle. Even though, atmospheric corrected datasets are used, the atmospheric influences might be only minimized and not fully eliminated. Therefore, a fixed band threshold applied to observations of all seasons and at global scale cannot account for the spectral variability of inland water bodies and varying atmospheric influence. In this study we use an approach that defines thresholds dynamically in space and time. This approach relies on training pixels that are identified for each MODIS tile and each observation date individually and that are used for a dynamic threshold definition, based on the frequency distributions of NIR and NIR-RED values within these areas. Subsequently, temporal analysis of the daily water mask sequence is used to interpolate for cloud and no data gaps and to provide a gap free time series of inland water dynamics.

The presented approach consists of five major steps which are illustrated in Fig. 2. In the 1st step, input data is processed and additional layers for masking possible water overestimation are generated (Section 3.2). Within the 2nd step, an automatic selection of training pixels is performed following defined criteria. In the 3rd step, dynamic thresholds for daily water classification are calculated for each MODIS tile and observation date individually based on the selected training pixels. Within the 4th step the daily MOD09GQ/MYD09GQ datasets are classified using the calculated dynamic thresholds and additional mask layers. The resulting water masks from Aqua and Terra datasets of the same day are combined in one layer and agreements or potential contradictions in classification results are assigned. In the 5th step, a temporal analysis of the daily water mask time series is performed to remove cloud and data gaps. The final results are daily gap free water masks, as well as a layer of confidence. In this study, the results for 2014 were quantitatively validated using high resolution Landsat reference data and were furthermore compared to the NRT NASA flood product for three selected flood events.

For the presented procedure, two thresholds (θ_A and θ_B , marked in red in Fig. 2) had to be determined. This was done based on a reference

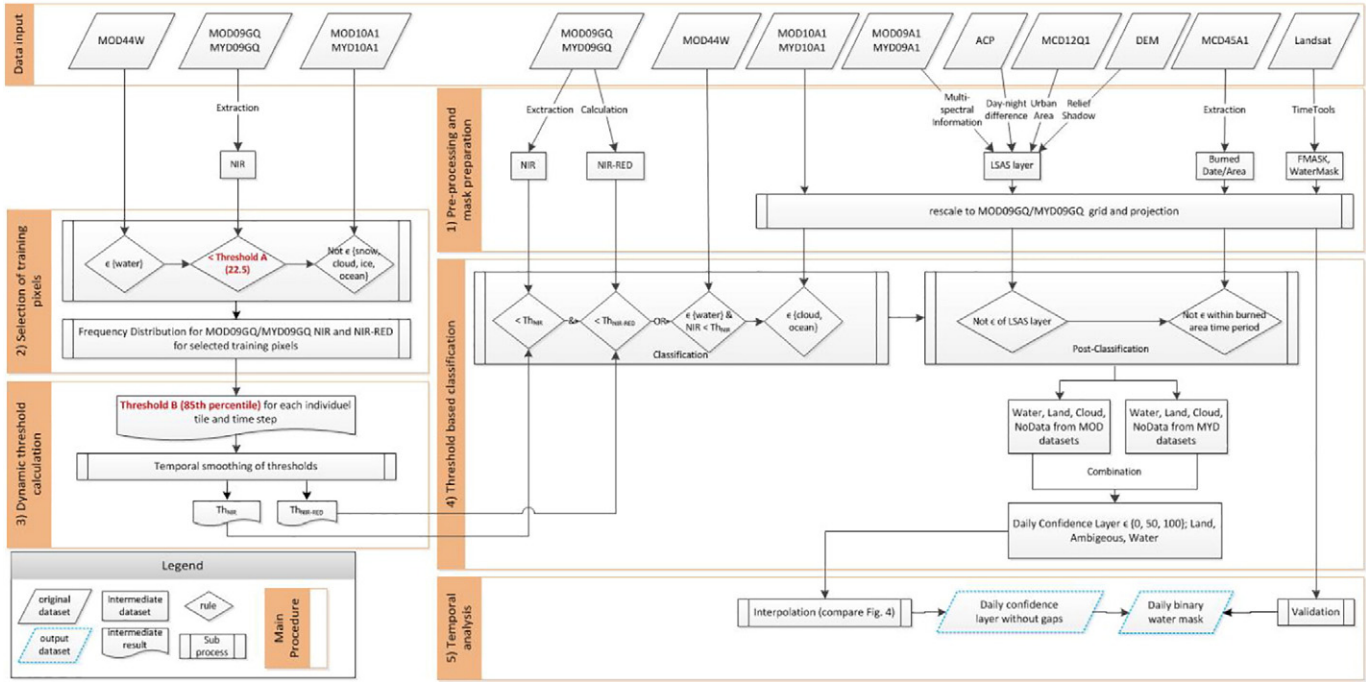


Fig. 2. Workflow overview for presented approach.

set of Landsat data (Section 3.3.3). Detailed descriptions of the individual processing steps and the threshold definition approach are presented in following sub-sections.

The GWP is not processed in a way to allow NRT applications as it requires time series analysis of one full year to exploit the temporal component. A cluster with 32RAM and 8CPU runs approx. 6 h for one tile and one year. Therefore a global processing of one year and ~15 TB of data takes ~50 days.

3.2. Pre-processing and mask preparation

3.2.1. Preparation of daily MODIS datasets

The NIR and red bands are extracted from MOD09GQ/MYD09GQ data and the reflectance difference (NIR-RED) is calculated by subtraction of red band from NIR band. The NIR-RED has proved to be an important input for accurate water detection (Sun et al., 2011). The 500 m snow cover layer from MOD10A1/MYD10A1 products was resampled to the grid of MOD09GQ/MYD09GQ to enable an automatic pixel based processing.

3.2.2. Generation of additional layers

A *Local Shadows and Ambiguous Surface Layer* (LSAS layer) was created to address misclassification errors related to topographic and building shadows and, e.g. dark land surfaces. This layer consists of information from different auxiliary datasets, whereas the source of information is labelled with unique values which allow addressing them individually within the later process. First, it contains slopes steeper than 5° inclination which were calculated from the global DEM by identifying gradients from each raster cell. Steep slope represent areas which are likely not covered by standing water but could be misclassified due to terrain induced shadows (Yamazaki et al., 2015). Nevertheless, steep terrain might embrace newly constructed dams. This is tackled by taking temporal relation into account which is explained in Section 3.3.2. Secondly, the urban class of MODIS classification MCD12Q1 was included to assign areas potentially affected by building induced shadows. Furthermore, the LSAS layer contains land surface areas, for example lava flows which might be misclassified as water. In contrast to shadows which occur depending on sun and sensor

geometry and seasonality, spectral ambiguous surfaces such as volcanic material can be misclassified throughout the year.

To target and identify these areas we utilized the long-term maximum temperature difference between day and night calculated from the ACP dataset. Land surfaces are usually characterized by stronger thermal diurnal variation compared to water bodies. Therefore, thermal data was used as an additional indicator to identify land surfaces with high diurnal day-night temperature fluctuations which were considered having a low probability of being water due to the high heat capacity of water. Identified ambiguous land surface areas went through manual interpretation and editing using multispectral information of corresponding MOD09A1/MYD09A1 products and GoogleEarth similar to the strategy introduced in the Algorithm Theoretical Basis Document (ATBD) of Copernicus Land Service for Water Bodies monitoring and other studies (Bertels et al., 2016; Copernicus GMES Initial Operations, 2013; Nigro et al., 2014; Pekel et al., 2014).

In contrast to areas identified by the LSAS layer where possible misclassifications occur at relatively stable geographical locations, spectral confusion can also occur on burned areas which are variable in location and time. Therefore, we extract dynamic layers of burn dates and locations of burn scars from the MCD45A1 product.

The LSAS layer and MCD45A1 product were resampled to the grid of the MOD09GQ/MYD09GQ datasets to enable automatic pixel-by-pixel processing.

3.2.3. Preparing of reference datasets

High resolution reference datasets for threshold definition (th_A and th_B marked red in Fig. 2) and validation were generated based on 321 Landsat images. The images were first atmospherically corrected using ATCOR software (Richter and Schlapfer, 2007) and classified using the *function of mask* (FMASK) approach (Zhu et al., 2015). The download, ATCOR and FMASK are implemented within the *TimeTools* module (Mack et al., 2017) which was used to execute this automatic process. The FMASK classification contains basic classes: water, land, lake ice, snow, clouds and cloud shadows. For each Landsat image, the quality of the water class in FMASK was checked by an image interpreter. If necessary the water class was improved based on specifically constructed decision tree classifications for each scene. Here individually defined

thresholds for band slicing in NDWI after Xu (2006) and band 7 (SWIR) were used for separating between land and water. These improved water classification were finally re-combined with all other classes from the initial FMASK classification (except for water). This procedure provided high resolution reference datasets with high accuracy of water class and additional information on clouds, cloud shadows and lake ice. Finally, the Landsat classification results were up-scaled and re-projected to fit the MODIS 250 m resolution using nearest neighbor method. Here the sub-pixel fraction of water was calculated for each MODIS 250 m pixel. In this way all input and additional datasets were matched to an equal spatial grid and tile system. The relatively high effort for generating this dataset was necessary in order to create an optimal reference dataset for a reliable validation and threshold definition.

3.3. Daily water classification

3.3.1. Selection of training pixels and dynamic threshold calculation

Pixels assigned as inland water in the static dataset MOD44W are considered as training pixel candidates. However, areas assigned as water in this static water mask are not necessarily covered by water in each of the daily MODIS observations because the MOD44W dataset mirrors a past time interval (Carroll et al., 2009). Water covered areas in such a dataset, might be – at the date of observation – dried out (e.g. shrinking lakes) or not covered by water due to seasonal fluctuations. Furthermore, they might be covered by clouds. There it has to be considered that cloud mask included in the MOD10A1/MYD10A1 datasets (originally from MOD35L2 product (Ackerman et al., 2006)) cannot guarantee the elimination of all cloud covered pixels especially on cloud fringes. There are also further technical reasons for pixels being distorted e.g. due to artefacts resulting from compositing processes, or sun glint.

Therefore, suspicious candidate pixels were excluded from the training set – for each tile and observation date individually – based on two criteria: training pixels may not be covered by clouds, snow, lake ice or ocean in the MOD10A1/MYD10A1 products, and they may not show too high NIR reflectances above a threshold-A (th_A) to exclude potential non-water pixels. The dynamic threshold for delineation between water and non-water pixels is then calculated based on the distribution of NIR and NIR-RED values within the remaining training areas. The 85th percentiles (th_B) of these distributions were used as upper thresholds (th_{NIR} and $th_{NIR-RED}$) to create daily water classifications (Section 3.3.2). These thresholds th_{NIR} and $th_{NIR-RED}$ derived on a

daily basis feature high variability from day to day due to several reasons e.g. difference of training sets due to high variability of cloud coverage and difference in data quality or distortion. Therefore the daily th_{NIR} and $th_{NIR-RED}$ are temporally smoothed using an 8-day-mean filter to minimize the noise. In this way, the seasonal development of spectral response of water is retained, but outliers are reduced as far as possible (Fig. 3).

3.3.2. Threshold based classification

Based on the smoothed thresholds th_{NIR} and $th_{NIR-RED}$ for each tile and observation date, the 250 m MOD09GQ/MYD09GQ datasets are classified into water, and non-water. A pixel is assigned as water when it features values below the dynamic thresholds of both NIR and NIR-RED, or if a pixel shows only NIR values below th_{NIR} but is assigned as water in the static mask. The second condition was included to avoid possible omission errors over permanent water bodies due to sun glint or data distortions. All pixels which are classified as non-water but are assigned as cloud or ocean within the MOD10A1/MYD10A1 products are labelled as such, remaining pixels are assigned as land. Subsequently the LSAS layer and the burned area layers (Section 3.2.2) are used to delimit areas where the temporal dimension is further inspected to determine the likelihood of a pixel being water. Pixels are re-classified to non-water where both the masks and the temporal profile indicate high probability of misclassifications due to relief and building shadows, ambiguous land surfaces and burned areas. In case of relief and building shadows, pixels are relabelled only when they show a seasonal variation because these shadows are seasonally dependent (Pekel et al., 2016). In this way, geographic location of possible relief and building shadows are combined with the temporal component. Practically, pixels which are classified throughout all clear observations within build up areas or within assigned mountainous regions remain classified as permanent water. In case of burned area the entire temporal interval when burned areas were detected are re-classified.

After classifying the individual datasets of MOD09GQ/MYD09GQ, the Aqua and Terra observations acquired at the same date are combined resulting in six classes: water detected by both sensors (water-water), land detected by both sensors (land-land), clouds present in data of both sensors (cloud-cloud), water-cloud combination, land-cloud combination, and land-water combination. As shown in Table 2, these classes are translated into a *Daily Water Confidence Layer* (DWCL) which indicates the confidence that a pixel is actually covered by water.

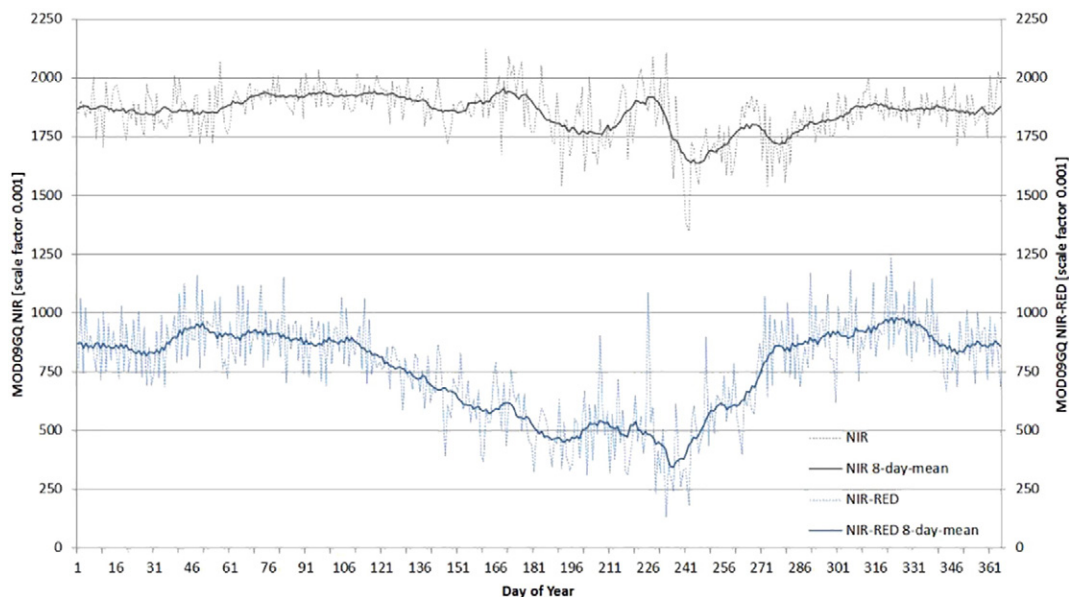


Fig. 3. Original daily and smoothed daily th_{NIR} and $th_{NIR-RED}$ (at 85th percentile) for 2014 (tile h26v06).

Table 2
Daily water confidence layer (DWCL).

Combined class Aqua + Terra	DWCL value	Description
Land-land	0	Least confidence: water
Water-water	100	Highest confidence: water
Cloud-cloud	50	Ambiguous
Land-cloud	50	Ambiguous
Water-cloud	50	Ambiguous
Land-water	50	Ambiguous

3.3.3. Determination of optimal thresholds A and B , and band combination

The daily classification step uses two fixed thresholds (th_A and th_B) as shown in Fig. 2. For identifying the best values for these thresholds applicable for global processing, a range of possible thresholds values were tested and compared against Landsat reference data. For th_A six NIR reflectance thresholds for excluding training pixel candidates were tested: $\leq 15\%$, $\leq 17.5\%$, $\leq 20\%$, $\leq 22.5\%$, $\leq 25\%$ and no threshold ($\leq 100\%$). For th_B nine threshold values were assessed. These thresholds are defined by percentiles of the NIR and NIR-RED value distribution of the selected training pixels: 50th, 65th, 70th, 75th, 80th, 85th, 90th, 95th, 99th percentile. Additionally, the performance of single band thresholding using only the NIR band, single band thresholding using only the NIR-RED, and the combination of thresholding in the NIR & NIR-RED band/index was tested. The threshold settings were tested for data of the year 2014 comparing results of 26 MODIS tiles with 50 Landsat footprints. The corresponding results using all possible combinations of the three variables (th_A , th_B , band selection) were evaluated based on random selection of 10,000 water and 10,000 land pixels from the each individual Landsat reference dataset. The performance of all tested threshold combinations and the choice of best thresholds is discussed in Section 4.4.

3.3.4. Temporal interpolation

With the aim to generate a gap free time series, the daily classification results (DWCL) require an interpolation for gaps resulting mostly from clouds or data artefacts. Based on time series analysis of the DWCL, all remaining data and cloud gaps and ambiguous classification results (DWCL-values of 50) were eliminated based on certain class assignments for previous and subsequent observations. The temporal analysis operates on the DWCL and generates a new *Daily Interpolated Water Confidence Layer* (DIWCL). In this way the memory of preceding detection (D'Andrimont et al., 2011) and the knowledge of subsequent detection is being used (Fig. 4). For dates featuring value 50 within the DWCL time series, a window with an initial size of 3 days is centered. The sum of all DWCL pixel values within the window excluding the centered pixel is divided by the amount of pixels within the window minus

one. The central pixel value is replaced by this new value. As long as the centered pixel has a value of 50, the window is resized by additional time step at the beginning and by additional time step at the end. This means that for some cases only few iterations are sufficient, whereas for others the moving window might propagate up to 33 consecutive pixels. When the moving window size reaches 33 time steps (one calendar month \pm one time step), the process truncates for reasons of efficient processing and the pixel is assigned to the class detected without ambiguity (value of 0 or 100) for the closest time step available. Additionally, the classification results are improved by filtering misclassification of *one day cases*. As a *one day case* we consider a pixel that has been classified only at one isolated day as water (land) but prior and after that time step as land (water). Such *one day cases* are identified in the time series and reinterpreted to the class that has been detected before and after. These kinds of one day cases occur for example in case of cloud shadows and in case of patch-type artefacts in MODIS data.

After executing this routine, all pixels within the generated DIWCL show values between 0 and 100 excluding the value of 50. Pixel values within the DIWCL can be considered as a measure of confidence for water detection. The calculated DIWCL values are used to reinterpret all cloud covered and ambiguous pixels of the DWCL. They are re-labelled to land when they show DIWCL values of less than 50 and to water when they show DIWCL values higher than 50. In this way, two outputs are provided, including a daily time series of cloud and gap free binary in-land water masks and a corresponding daily confidence layer (DIWCL). The DIWCL assists for a better interpretation of the results. The higher (lower) the value within the DIWCL, the temporally closer cloud free and unambiguous classification of water (land) at both sensors was used to interpolate for that gap.

Finally, the number of water classifications within the time series of daily binary masks are counted for each year resulting in annual water cover duration layer (AWCDL) which represents the amount of days on that one pixel was covered by open water.

3.4. Validation

The generated daily water masks are validated based on the 321 Landsat reference classifications described in Section 3.2.3. From these reference datasets 10,000 water and 10,000 land pixels were randomly selected from each scene and cross compared with the corresponding pixels in the GWP. In some cases the validation scenes did not contain enough water pixels to provide 10,000 samples. In these cases, a fraction of 25% of available water pixels was randomly selected. Here, pixels that have been formerly used for the definition of th_A and th_B (Section 3.3.1) were excluded from sampling. Furthermore, only Landsat-based reference pixels (scaled to the 250 m MODIS grid) with a water sub-pixel fraction of more than 50% were considered as water validation samples, while pixels with a land sub-pixel fraction of more than 50% were

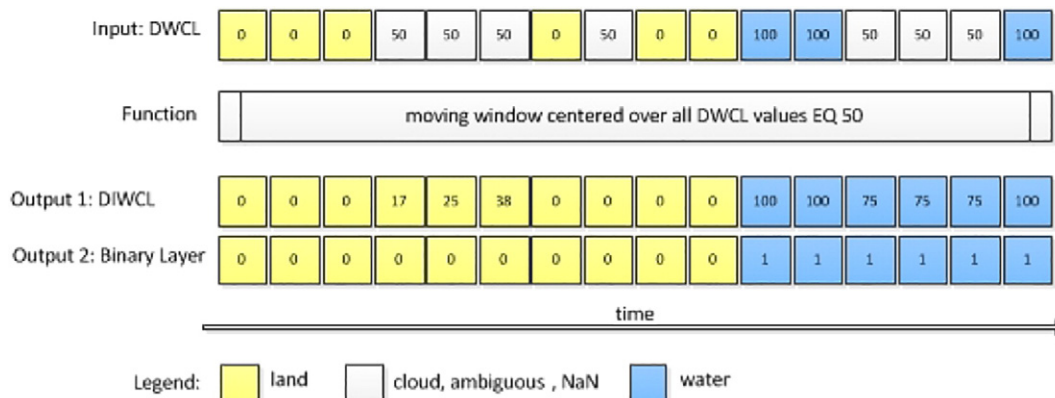


Fig. 4. Temporal interpolation and gap removal for one pixel.

considered as land validation samples. Error matrices as well as kappa coefficients were calculated, which has been widely accepted as standard for quantifying accuracy (Congalton and Green, 2008; Foody, 2006; Klotz et al., 2016).

Secondly, we compared the generated daily water information with the NRT NASA 2D MWP and with our detailed Landsat reference classifications for three major flood events of the year 2014 for the time interval of these floods as well as pre-flood and post-flood situations. The NRT NASA 2D MWP product aims at near real time flood detection especially of large scale floods and is also based on MODIS data. It contains four classes: no water, reference water, flood water and no data. Three

flood events were selected to compare both datasets (Amazonas on 4 Sep. 2014, Rio Mamoré on 15. Apr. 2014, River Sava on 22. May 2014).

4. Results

At the beginning of this section we discuss the results of selection of thresholds th_A and th_B which were tested for different clusters before processing on global scale (Section 4.1). In Section 4.2 results of the AWCDL are presented. Section 4.3 discusses the daily resolution water masks and highlights the potential of the high temporal resolution

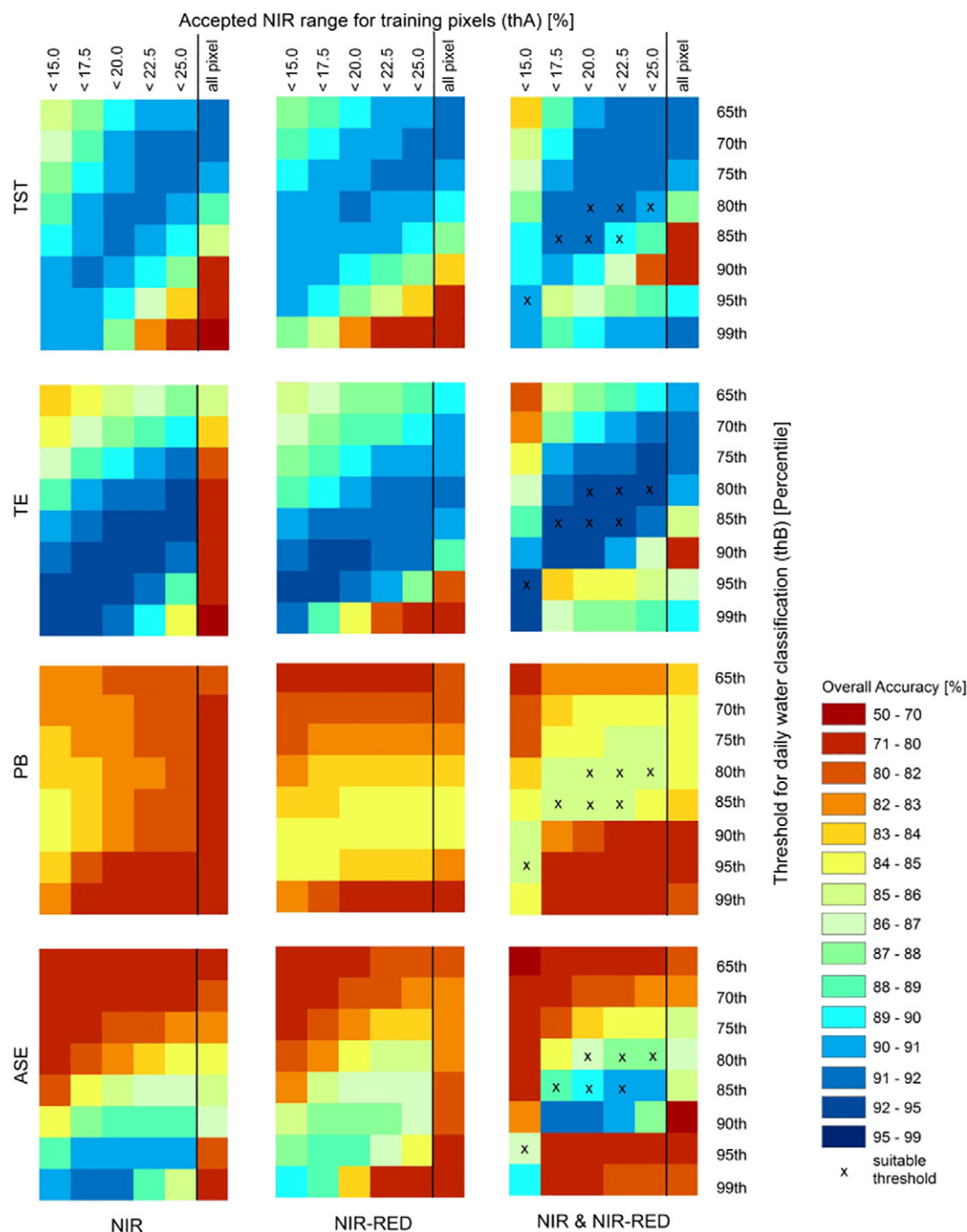


Fig. 5. Overall accuracies attained for water delineation when using different combinations of values for th_A (x-axes of matrices), and th_B (y-axes of matrices), based on only NIR (left column), on only NIR-RED (center column) and on a combination of NIR & NIR-RED (right column) for four clustered biomes (ASE, PB, TE, TST).

dataset. In Section 4.4 the validation results and comparison with other products are presented.

4.1. Definition of thresholds th_A and th_B

The test results for the determination of optimal thresholds th_A and th_B , as discussed in Section 3.3.3, are presented in Fig. 5. The twelve matrices of Fig. 5 show overall accuracies as achieved for different combinations of th_A -values, th_B -values, with different input features, and for different global regions. Each row of matrices represents one of the considered four major global regions (TST, TE, PB, ASE; compare Fig. 1). The first column of matrices shows accuracies that were achieved when only NIR was used as input feature, while the second and third column show results when using NIR-RED, and a combination of both features, respectively. NDVI was not included in this analysis due to the fact that the used datasets feature negative values above water bodies. Within affected areas it leads to errors due to deviation operation. Negative values appear irregularly and not systematically in NIR as well as in red channels. It occurs that both channels feature negative values or only one of them. The reason can be found in the atmospheric correction algorithm which was developed mainly for land surface (Vermote et al., 2011). Within each single matrix the overall accuracies for different combinations of tested threshold values for th_A (x-axis) and th_B (y-axis) are shown in color.

By comparing the three columns of matrices (Fig. 5) the performance of the chosen bands/indices and their combination can be assessed. When using only the NIR band (left column Fig. 5) good results can be achieved for all regions except for the polar and boreal areas (PB). One of the reasons for low NIR-based accuracies in the PB are low sun angles at high latitudes during the winter period and thus a decreased separability between water and some land surfaces within the NIR band. When using only NIR-RED (mid column Fig. 5) the results show higher accuracies for the PB regions as this index is less sensitive to illumination conditions. On the other side, the use of NIR-RED is

only appropriate for water detection, when clouds, snow and salt pans are not present or perfectly masked because these features, similarly to water, have very low NIR-RED values. Even though snow and cloud masks are used in the presented approach, these do not perfectly exclude all cloud and snow pixels. Using only NIR-RED therefore leads to inaccuracies at global scale (e.g. in PB regions). Using both NIR & NIR-RED in combination (right column Fig. 5) provides best overall results consistently over all four regions and minimizes the mentioned drawbacks of single NIR band and single NIR-RED usage. The advantage of NIR-RED being less sensitive with regards to illumination in combination with NIR which allows excluding all bright land surfaces and remaining (non-masked) cloud contaminated pixels proves to be more stable for the considered global reference set. Therefore, the NIR & NIR-RED combination was finally chosen for global processing.

When assessing the accuracies achieved for the considered threshold combinations, it becomes evident that in most cases there is a tendency towards negative relation between th_A and th_B values: the higher th_A , the lower is the th_B value that leads to optimal results. However, there is not one particular threshold combination which performs best for all considered regions.

Aiming at a globally applicable approach, our goal was to select one combination of th_A and th_B which yields optimal and stable results for all regions. This was determined by searching for the th_A and th_B combinations with optimum accuracy for all regions. As the PB region generally showed the lowest accuracies, it was decided to select only among those threshold combinations that provide overall accuracies of at least 85% - i.e. best values attained for PB - in all regions. Within this accepted range seven threshold combinations were suitable for all regions (marked by x symbol in Fig. 5). That means there is more than one applicable combination due to mentioned dependency between th_A and th_B . Based on the outcome of performed analysis th_A of 22.5% and the 85th percentile for th_B as well the usage of combination of NIR & NIR-RED was set as a default for performed water-land delineation.

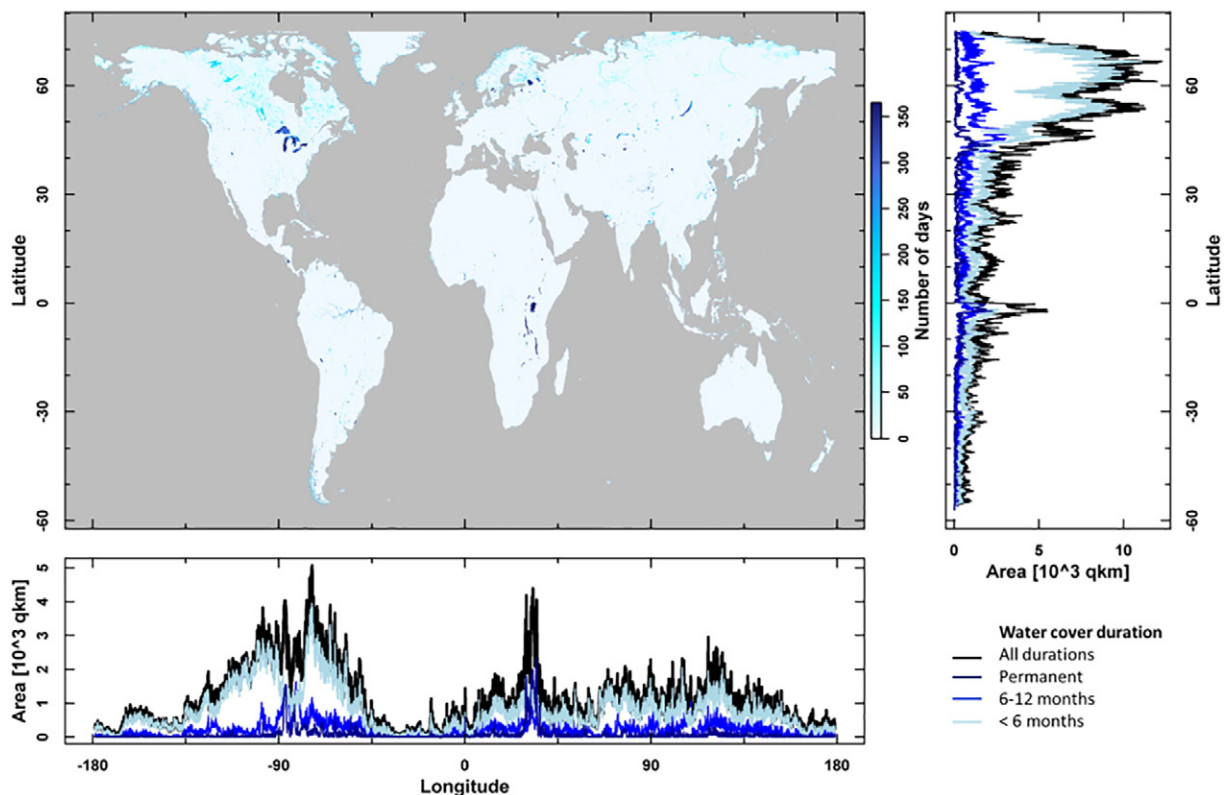


Fig. 6. Global water distribution for 2014. Areal summaries for four temporal categories of open water surface cover duration (black = all durations, dark blue = 365 days, blue = 180–364 days, light blue = 1–179 days).

4.2. Annual water cover duration layer

The global distribution of open water cover duration in the year 2016 is displayed in Fig. 6. The plots in Fig. 6 distinguish four categories of open water cover duration. The overall distribution pattern of total detected amount corresponds to previous work and results derived from coarser resolution (Papa et al., 2010) and finer resolution (Pekel et al., 2016; Yamazaki et al., 2015). In total for 2014 3.82 km² were classified as water at some time. This number also matched the results presented by Pekel et al. (2016) who found out that in 2015 3.59 million km² were covered by water at some time. The discrepancy

between different products is probably due to spatial resolution difference and the corresponding mixed pixel effects as also stated by Yamazaki et al. (2015). Latitudes higher than 30°N show a peak of water cover with majority of water pixels features freezing cycles. The peak of permanent water around equator mirrors the water of Amazonas and Victoria Lake.

Figs. 7 and 8 show the AWCDL 2014 for selected areas and lakes in North and South America, Siberia, Central Asia and South-East Asia. In terms of lakes around the Lake Superior it is obvious that water bodies freeze during winter periods with very low temperatures. These freezing and thawing dynamics of waterbodies in the north of North America

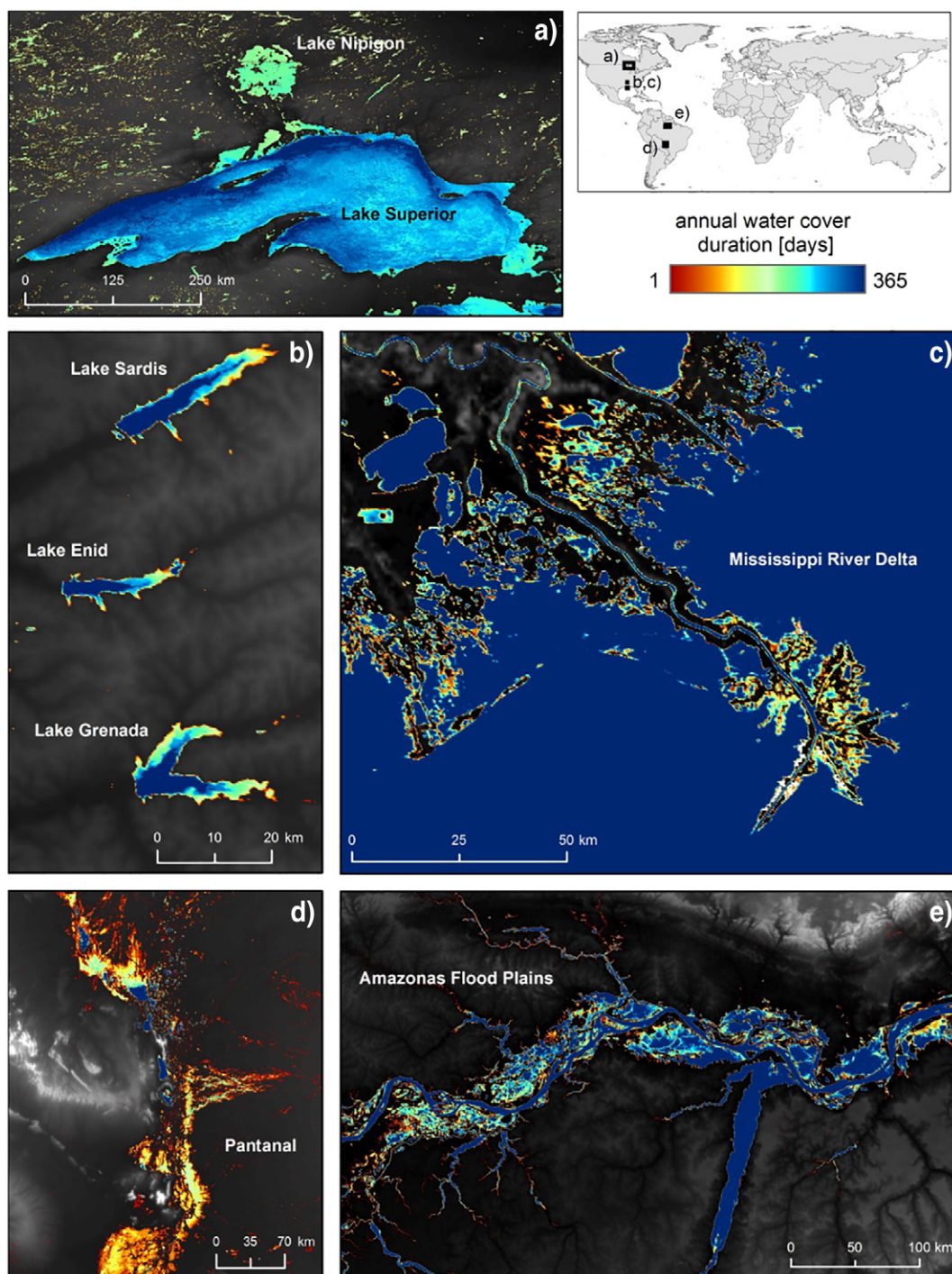


Fig. 7. GWP, Annual Water Cover Duration Layer 2014 for Lake Superior, USA (a), Lake Sardis, Enid, Grenada, USA (b), Mississippi River Delta, USA (c), Pantanal, Bolivia and Brazil (d), Amazonas Flood Plains, Brazil (e). Background: regionally stretched DEM.

and Siberia are reflected in the GWP dataset (Figs. 7a, 8a). Likewise, AWCDL captures the seasonal inundation and drying dynamics of lakes as well as the seasonality of lakes and reservoirs (Figs. 7b, 8b and d). Temporal inundation caused by high river discharge can be seen in Figs. 7d, e and 8a, d as well as high surface water dynamics in river deltas (Figs. 7c, 8e).

4.3. Time series of daily water masks

Fig. 9 depicts the development and retreat of an inundation of the Zambezi River in Caprivi Strip (Namibia). The top three rows of Fig. 9 show the fast flooding of vast areas within only few days. The bottom three rows of Fig. 9 show the flood retreat. This example highlights that the daily information provided by the GWP can contribute to a better understanding of surface water dynamics and build an information basis e.g. for flood and inundation regimes.

4.4. Accuracy assessment and comparison with other datasets

In Fig. 10 the daily GWP results are compared to the Landsat-based reference datasets (Section 3.2.3) for Lake Urmia, Iran. The visual comparison shows that the seasonal drying out and flooding of the lake is well detected in the GWP when compared to the Landsat reference. The 250 m MODIS product is able to capture the spatial and temporal

patterns as detected in the high resolution reference data. However, an underestimation of very small lakes and narrow rivers which are clearly below the spatial resolution of MODIS can be observed. It should be noted that the areas classified as ice in the Landsat-based FMASK results are actually misclassifications of salt pans and clouds.

Another comparison showing the potential of the high temporal resolution of the GWP is presented in Fig. 11. The maps of two reservoirs, the Sharda reservoir, Kazakhstan, and the American Falls, USA provide information on how long a pixel was covered by water within the year 2014 (AWCDL layer). The plots (Fig. 11a and b) contain information on the temporal development of the reservoirs water surface extents throughout the year 2014. They show when the reservoirs dried out or froze, and when they refill or unfroze, respectively. Fig. 11a includes in-situ measured water surface levels provided by the Ministry of Environment Protection of the Republic Kazakhstan and Fig. 11b includes in-situ measured information of the reservoir water surface elevation (Bureau of Reclamation of the U. S. Department of the Interior, 2016). The plots clearly show that the reservoirs experience high temporal variations throughout the year and that the variations of the reservoirs of the reservoirs are well captured by the daily water surface detected by the GWP.

Fig. 12 shows a comparison of the AWCDL for 2003, 2009 and 2014 and a selection of other available static water body products, again focusing on Lake Urmia, Iran. The gradual shrinkage of the lake as well

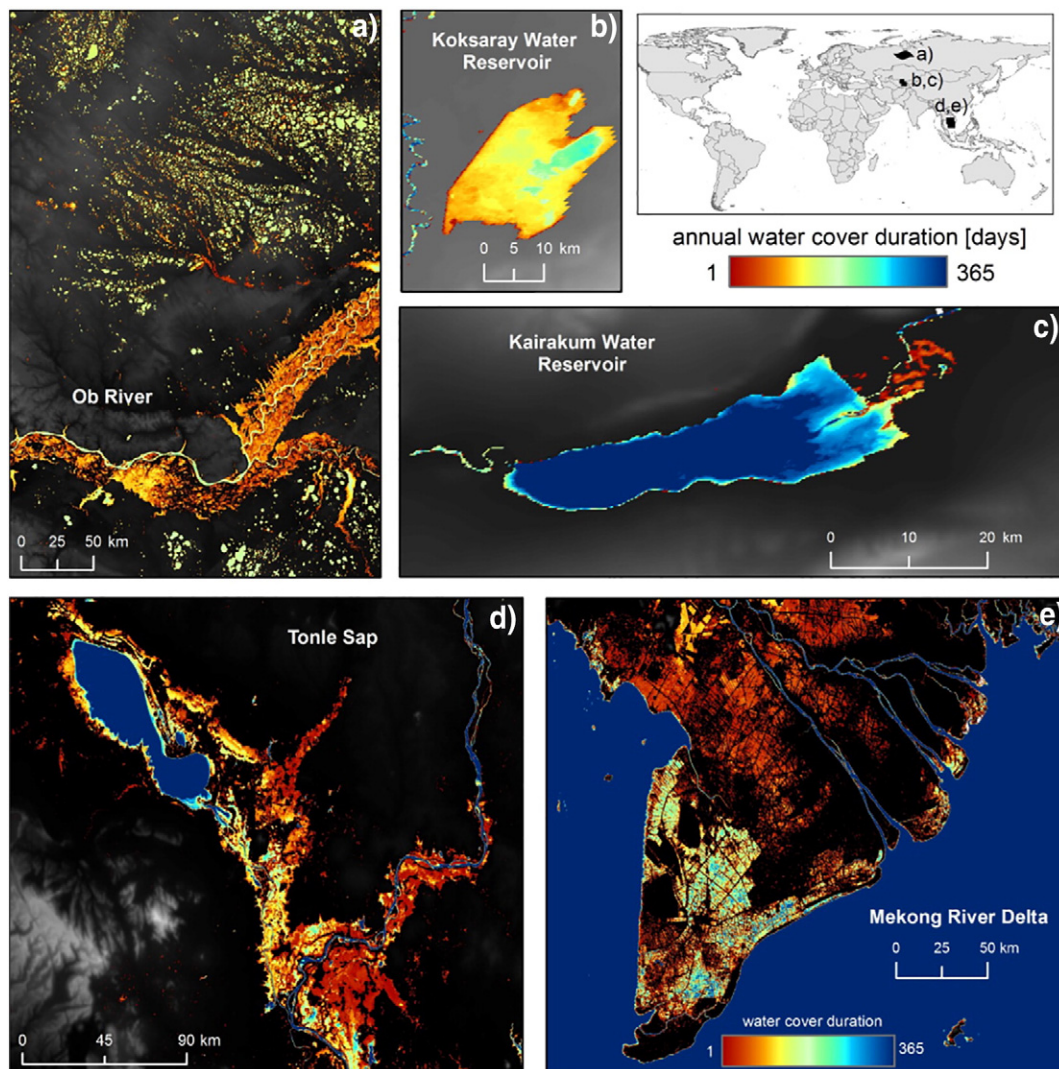


Fig. 8. GWP, Annual Water Cover Duration Layer 2014 for parts of Ob River, Russia (a), Koksaray Reservoir, Kazakhstan (b), Kairakum Reservoir, Tajikistan (c), Tonle Sap, Cambodia(d), Mekong River Delta, Vietnam (e). Background: regionally stretched DEM.

as the intra-annual variability (as presented in figure) is well detected by the GWP. The static products mirror the permanent and, in case of G3WBM, the seasonal water extent, but do not give any detail on the inter-annual and multi-annual spatio-temporal patterns of such a shrinking lake.

The results of the quantitative accuracy assessment (comparison with 321 globally distributed Landsat reference datasets) are summarized in Table 3. The overall accuracy for 250 m pixels with a sub-pixel water fraction of 100% is 96.3% with Kappa coefficient of 93.3. For reference pixels with a sub-pixel water fraction of 75–99.9%, the overall accuracy is 90.1% (Kappa = 79.3). For sub-pixel water fractions of 50–74.9%, an overall accuracy of 58.7% (Kappa = 15.4) could be achieved.

The decrease in accuracy with decreasing sub-pixel water fractions is due to mixed pixel effects occurring at the medium spatial resolution of 250 m. Thus, especially narrow rivers, channels and very small water bodies are underestimated which is mirrored in an elevated omission error of 72.4% for low sub-pixel fractions of water (50–74.9%).

Focusing on selected flood events in 2014, Table 4 presents the quantitative accuracy assessment results for the GWP and the NRT NASA 2D MWP in comparison to high resolution Landsat reference datasets. The results show that the presented approach is capable to capture flood events and achieves higher accuracies than the results of NRT 2-day composites. However, it has to be considered that the NRT processing aims at fast and rapid flood detection, whereas the GWP

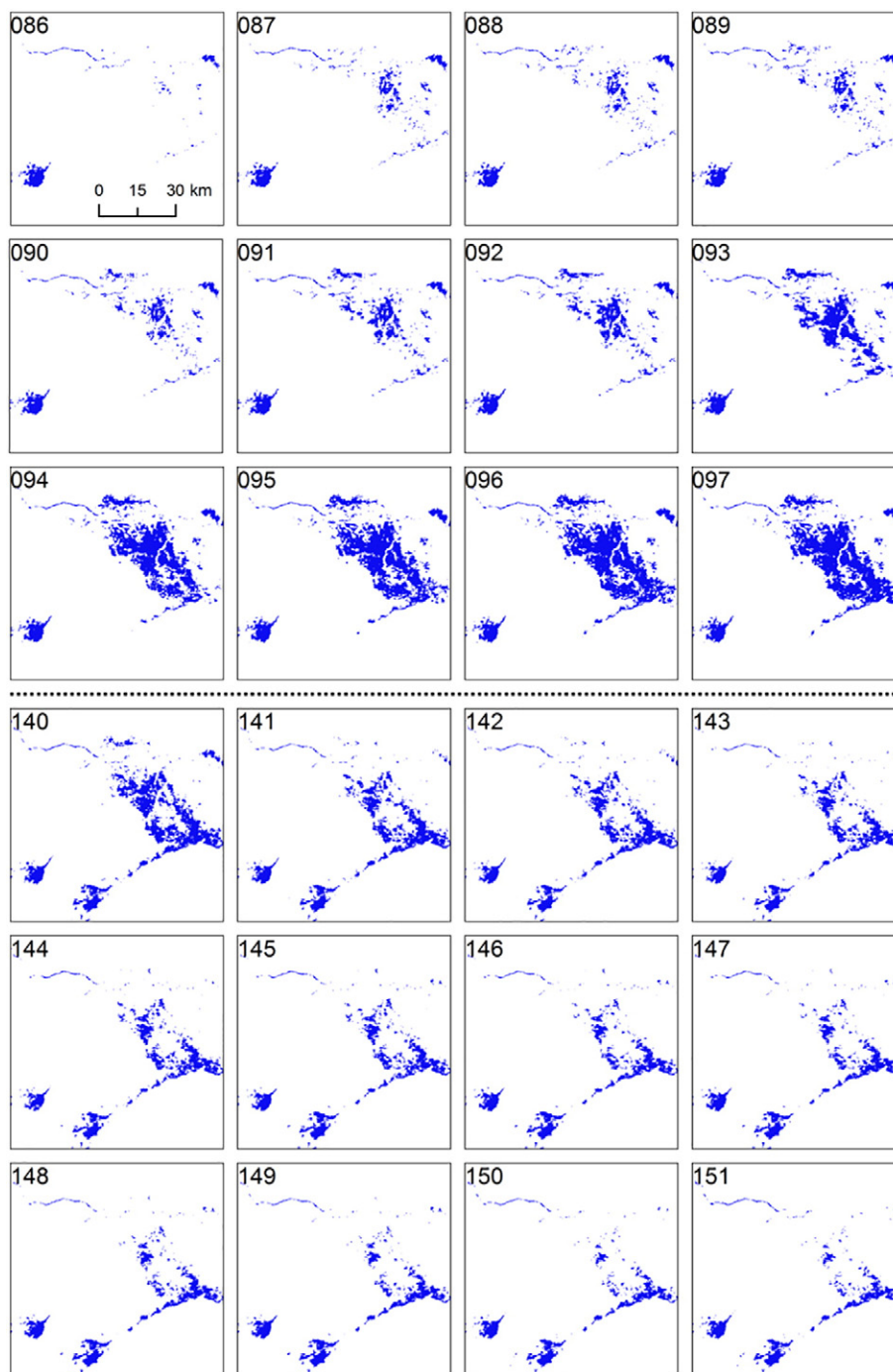


Fig. 9. Daily surface water classifications reflecting the rising and retreat stage of floods of the Zambezi River. The numbers in the top-left corner indicate the day of year. DOY 86–97 (27/03/2014–07/04/2014): flood expansion period. DOY 140–151 (20/05/2014–31/05/2014): flood retreat period.

aims to reconstruct the surface water history with high temporal resolution and continuity exploiting the time series of classified results to analyze water body dynamics in a geoscientific context.

5. Discussion

5.1. Potential and limitations

The GWP's clear advantage over existing datasets is its high level of detail revealing the spatio-temporal variability of inland surface water. In this way, the product represents the variability of e.g. shrinking and filling up water bodies. The comparison with the NRT NASA 2D MWP product proved that the approach is for example capable of detecting

the progress of inundation and recession. The comparison with 30 m resolution reference datasets also confirmed the achieved detail at spatial and temporal scale. However, as for all surface water datasets derived from multi-spectral sensors the presented approach has certain limitations. First of all, it is designed to detect only open water surfaces, while water bodies which are covered by vegetation are not captured. Examples are swamps, inundated dense forests or areas of water bodies with floating vegetation. The detection of extremely turbid and highly eutrophic waters, where NIR reflectances can be higher than red reflectances, is also limited. Additional indices or fusion with radar data could in future be used to reduce these omission errors. Secondly, the utilized additional datasets for identification of potential areas of commission errors might also introduce some limitations due to their own

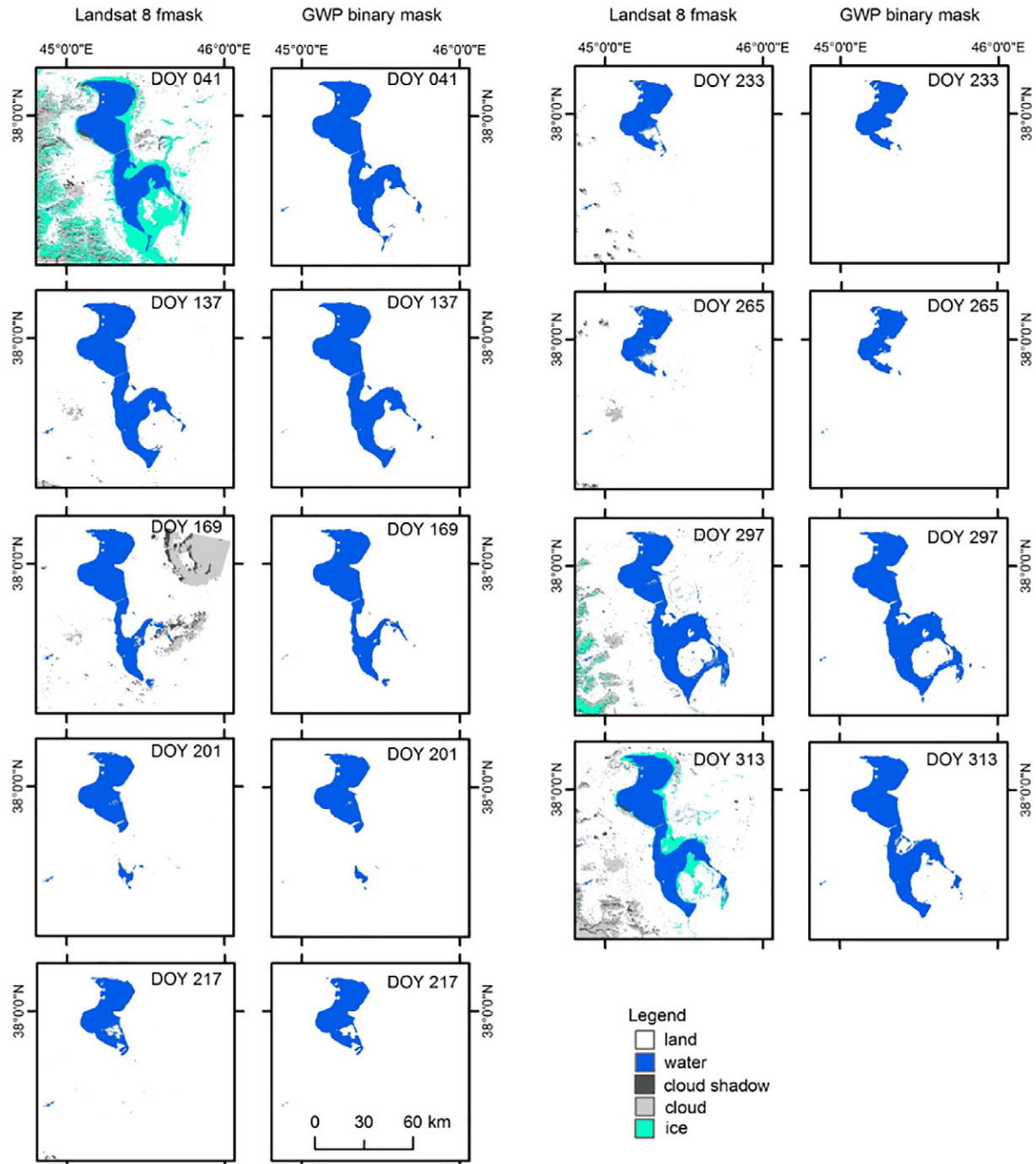


Fig. 10. Comparison of GWP with Landsat classification reference sets of Lake Urmia, Iran for selected days of year (DOY) in 2014.

product limitations. For example in terms of urban fast spreading some urban areas might be still not classified. Furthermore, it has to be considered that, frozen water surfaces are not classified as water in the GWP which can be a limitation for some application but at the same time it allows to analyze freezing and thawing cycles. The freezing and thawing dynamics captured by presented approach might allow further research on freezing and thawing of lakes at daily temporal resolution which might be of high interest e.g. for ecological and hydrological

climate impact research. The GCOS 2016 Implementation Plan requires water extent and lake ice coverage products for lakes with daily resolution and 20 m and 300 m spatial resolution respectively (WMO, 2016). Therefore, the presented approach and dataset might be of a new value at least towards the temporal resolution.

It has been shown that the GWP dataset detects pixels with high sub-pixel fractions of water more accurately than pixels with lower water fractions. Especially the classification of narrow rivers and small

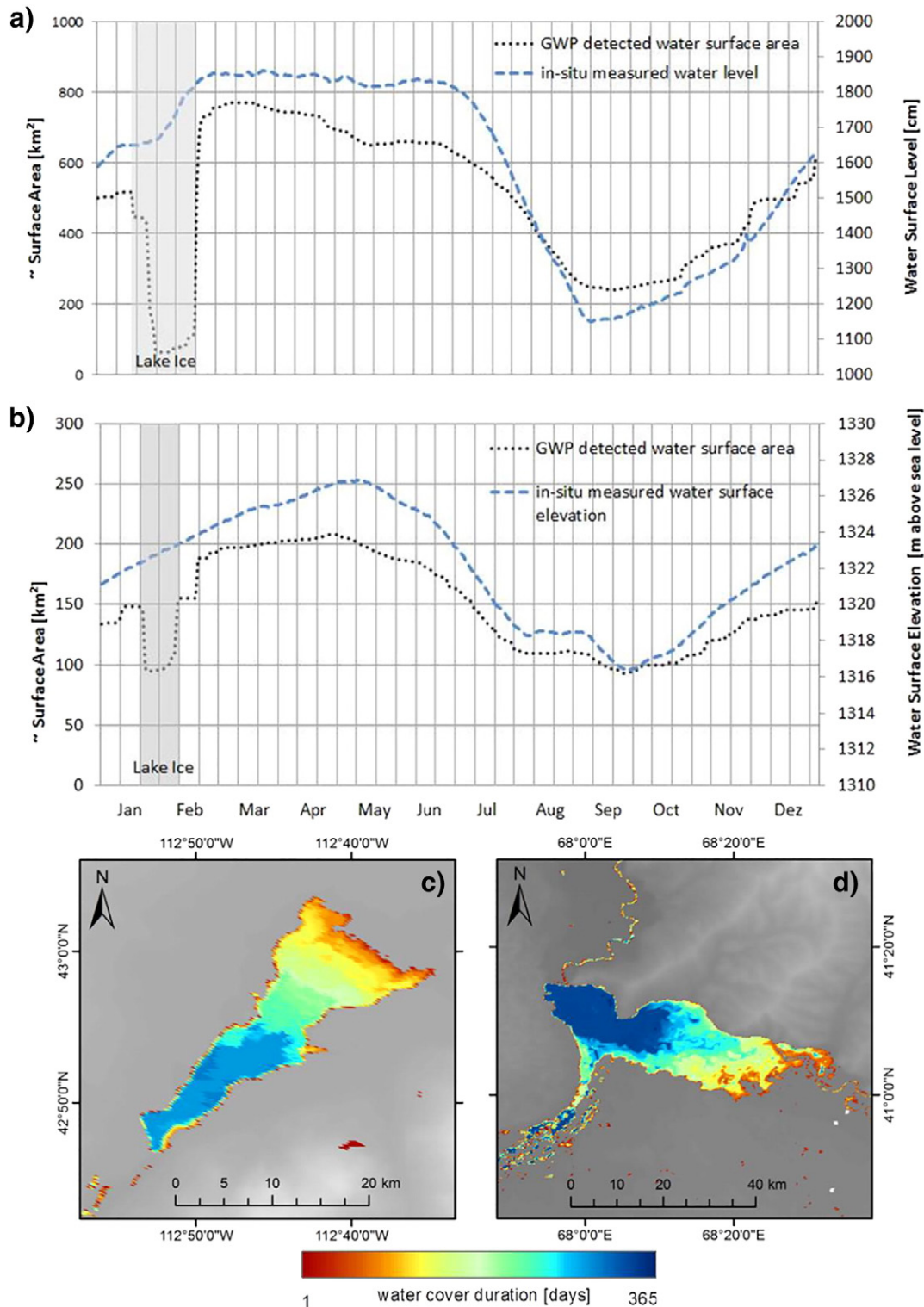


Fig. 11. Temporal development of water surface area of the for Shardara Reservoir, Kazakhstan (a) and for American Falls Reservoir, USA (b) and the overview maps (AWCDL) of the two water bodies (c, d).

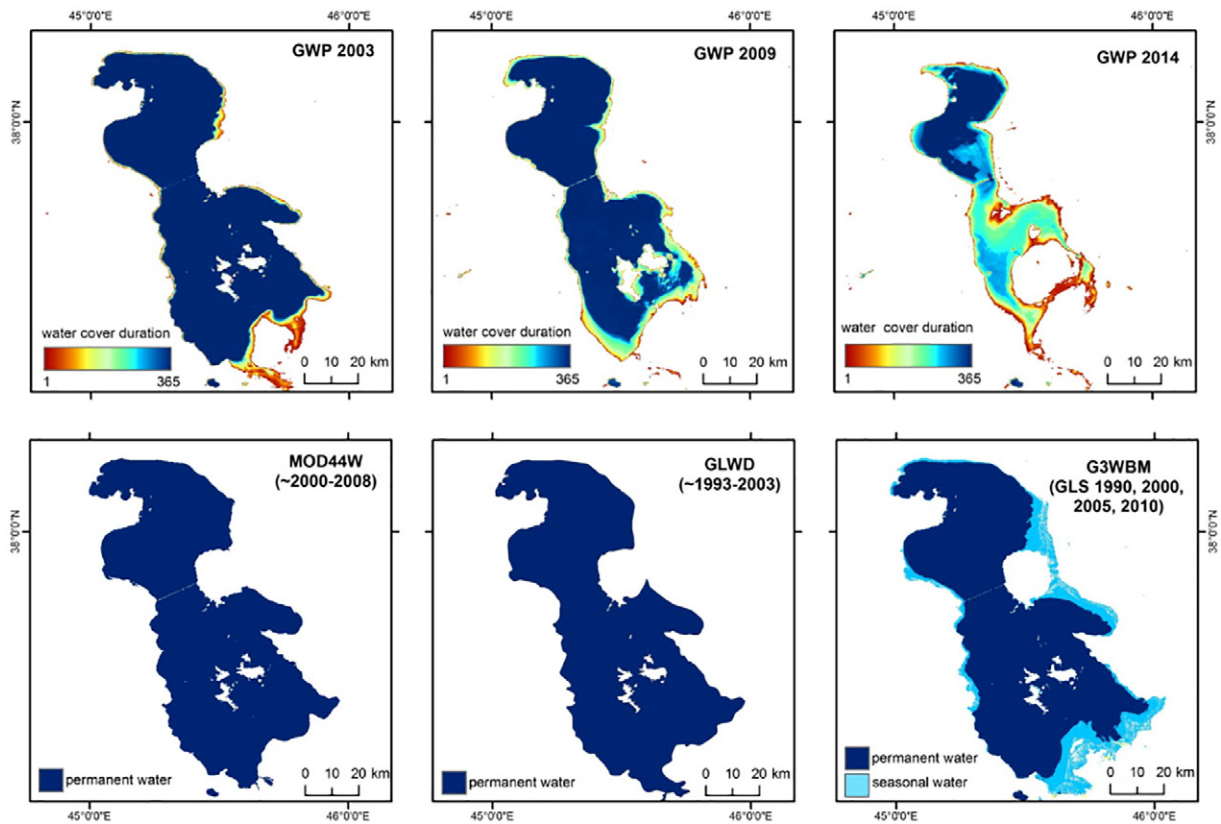


Fig. 12. Comparison between Global WaterPack AWCDL 2014 and selected static water body products, for Lake Urmia, Iran.

water bodies is affected by the mixed spectral response of pixels with different land cover types as already demonstrated by many studies (Guerschman et al., 2011; McCullough et al., 2012; Ticehurst et al., 2014). This also implies that the potential of this global product lies in the assessment of larger-scale water body dynamics rather than of small size lakes and narrow rivers below the spatial resolution of MODIS. An analysis of small scale dynamics would require higher resolution datasets based on Landsat or Sentinel-2 data (Pekel et al., 2016; Sheng et al., 2016) but in this case the temporal frequency would be lower (Yamazaki and Trigg, 2016).

In this study we applied complimentary threshold settings of th_A and th_B on global scale. The overall accuracy for all regions reached at least 85%, although it should be noted that a regionally optimized threshold setting of th_A and th_B might still increase the level of accuracy for certain regions. On the other side, the accuracy in challenging regions such as urban or mountainous areas with small water bodies, narrow rivers (compared to MODIS pixel size) might be lower. Furthermore, regions which cannot be observed by optical sensors for longer time period (pixels affected by Polar winter and tropical high cloudy regions with cloud coverage for almost entire year) might be not classified correctly based on only few observations. Here SAR imagery might be used in addition to maximize the product's reliability. Even though the snow, cloud and lake ice classification of the MOD10A1/MYD10A1 products were used within the approach it should be noted that, this information was only applied supporting the selection of training pixels. The spectral information for creating the daily classifications however, are the spectral datasets MOD09GQ/MYD09GQ. In this way, it was possible to also map water in areas even if these were assigned as cloud in MOD10A1/MYD10A1. Furthermore, the GWP is only produced for land pixels of MOD10A1/MYD10A1 (as only here the necessary cloud masks are available). This introduces some limitations along coast lines, particularly in areas of considerable land accretion.

Recently, many Landsat based studies demonstrated valuable and high spatial resolution results on global surface water mapping (Feng

et al., 2015; Pekel et al., 2016; Yamazaki et al., 2015). Studies on continental scale using the entire Landsat archive and analyzing the temporal variability of inland water bodies show great potential for different applications (Mueller et al., 2016; Ticehurst et al., 2014; Tulbure et al., 2016). Especially, Pekel et al. (2016) introduces a set of thematic products depicting water persistence and seasonality on global scale. This work is a mile stone in optical remote sensing of surface water mapping due to the combination of high spatial resolution data, and time interval of 32 years exploiting the Landsat 5, 7 and 8 archives. However, the 16-day repeat cycle of Landsat, cloud cover and data gaps affect the seasonality information (Yamazaki and Trigg, 2016). Nevertheless, the fact that Landsat has revisit times of 16 days (8 days when two satellites operate at the same time), and cloud coverage is still a major issue, there might be temporally long gaps between two clear observations. Furthermore, Landsat archive features some data gaps and temporal discontinuities depending on geographical location (Pekel et al., 2016; Yamazaki and Trigg, 2016). Even though cloud coverage is also a major issue for products derived from bi-diurnal optical data such as MODIS, the probability of obtaining cloud free observations is higher. The presence of cloud coverage over several days can be tackled by temporal compositing using best observation within a certain time interval. The usage of

Table 3

Global accuracy assessment for different sub-pixel fractions of water. Presented values are average values for the entire globally distributed Landsat-based reference dataset.

	Sub-pixel water fraction within MODIS 250 m pixel		
	100%	99.9–75%	74.9–50%
Omission error	7.8%	20.7%	72.2%
Commission error	0.5%	0.9%	13.1%
Water mapping accuracy	91.7%	78.5%	23.1%
Overall accuracy	96.3%	90.1%	58.7%
Kappa coefficient	93.3%	79.3%	15.4%
F-score	95.4%	86.6%	35.6%

Table 4

Comparison between GWP daily and NASA NRT 2 day composite results.

	Accuracy NRT	Accuracy GWP	Omission NRT	Omission GWP	Commission NRT	Commission GWP
Amazonas (h12v09)	35.35%	98.94%	65.34%	2.99%	0.86%	20.97%
Rio Mamoré (h11v10)	61.57%	87.54%	43.89%	20.23%	27.63%	1.91%
River Sava (h19v04)	88.37%	92.16%	12.62%	8.87%	66.35%	9.40%

temporal composites from eight days up to one month has been proven to be very useful for land cover mapping and surface water detection and is suited for many applications. However, if we want to understand the reaction and sensibility of water surfaces on finer temporal scale, daily information is required. Furthermore, as stated by Guerschman et al. (2011) in their case study, the results derived from composite data can miss some or all standing water compared to results from daily data.

5.2. Potential applications

The major advantage of the GWP product compared to existing datasets is its high temporal resolution. This daily dataset can for example improve calibration, assimilation and validation of climate and hydrological models with typically high temporal resolution. It can furthermore support water level measurements with radar altimetry where algorithms greatly benefit from day-specific information on the presence or absence of open water surfaces. The daily temporal resolution of the GWP can reveal new insights into the impact of climate change, meteorological variability and human activities on surface water dynamics, freezing and thawing cycles, freshwater availability and respective implications for ecosystems and human livelihoods. Areas prone to floods can be identified and combined with information on meteorological events to estimate the probability of inundation. Also for supporting water management decisions, the GWP can provide suitable information that complements commonly available datasets such as in-situ and radar altimetry measurements of lake and reservoir levels (Schoene et al., 2016). Here, the presented product can contribute spatially explicit information when a reservoir empties and fills (e.g. in average or extreme years) and how it reacts to different influences such as droughts, extreme precipitation, snow melt and water management. In this way reservoir dynamics and hydropower can be combined and analyzed. These results might allow further environmental investigations and tackle many research questions in the context of inland surface water variability (hydrological regimes, influence of precipitation and snow melt on natural and artificial inland water bodies, role of population increase, and relation to certain diseases). As lakes and reservoirs are threatened by the synergistic effects of multiple, co-occurring environmental pressures (Palmer et al., 2015) research questions focusing on environmental and climate changes and the sensibility of open surface waters might reveal new insights. Such applications will provide results of high importance when analyzing the entire MODIS archive and the resulting long time series of water body dynamics.

In the future, a fusion of temporally dense GWP and high spatial resolution datasets derived from Sentinel-2 or Landsat might lead to even higher information contents.

6. Conclusion

The Global WaterPack product is based on bi-diurnal moderate resolution data and auxiliary information using a dynamical thresholding of the difference index (NIR band – red band) in combination with the NIR band. The results have been validated based on 321 Landsat images and show very high overall accuracy for pixels fully covered by water (96.3%), high accuracy for pixels with water fraction of more than 75% (90.1%) and medium accuracy for pixels which feature higher land fraction than 25% (58.7%). Furthermore, a comparison with products derived within a MODIS based near real time service underlines the

reliability of applied approach. Presented examples reveal the potential of a dataset with high temporal resolution. Especially, water reservoirs, lakes in endorheic basins or flat terrain feature rapid changes within few days which depend on human water regulation, snow melt and precipitation. Additionally, freezing and thawing cycles around the globe can be examined at daily resolution as required by WMO (2016). In combination with additional data (e.g. temperature) the beginning, ending and period of freezing cycles could be assessed. Furthermore, the Global WaterPack enables investigating the impact of natural versus human driving factors on reservoirs and lakes in more detail. Based on high temporal resolution data it might be possible to investigate the sensitivity and reaction of lakes and reservoirs towards climate, land use, and environmental changes.

At the moment the years 2013–2015 have been processed completely, whereas processing of the entire MODIS archive back to July 2002 is ongoing. Future research could focus on transferring the method to other moderate resolution data to ensure a continuous reconstruction of inland water development further into the past and future. The approach can be transferred to data such as of Visible Infrared Imaging Radiometer Suite (VIIRS) on board of Suomi National Polar-orbiting Partnership (NPP) or data of Ocean and Land Colour Instrument (OLCI) on board of Sentinel-3A and B. Expanding the time series will reveal more information with regard to trends related to climate and environmental changes and human impact. This holds a large potential for a broad range of geoscientific analyses and applications. Recent water mapping achievements based on high resolution data archives such as Landsat can be combined with the results of high temporal resolution datasets presented here to overcome data and cloud gaps and reveal the water body variability and research for driving keys factors and the sensitivity of water bodies on finer temporal and spatial scale.

Acknowledgements

The authors would like to thank NASA, NOAA, USGS and NSIDC for providing download services and all datasets free of charge. We thank Benjamin Bechtel for providing the ACP dataset, and CGIAR CSI for providing the global DEM. Furthermore, we highly appreciate valuable and constructive comments on the manuscript provided by the anonymous reviewers.

References

- Ackerman, S., Strabala, K., Menzel, P., Frey, R., Moeller, C., Gumley, L., Baum, B., Wetzel, Seemann, S., Zhang, H., 2006. *Discriminating Clear-sky From Cloud With MODIS Algorithm Theoretical Basis Document (MOD35)*.
- Bechtel, B., 2015. A new global climatology of annual land surface temperature. *Remote Sens.* 7:2850–2870. <http://dx.doi.org/10.3390/rs70302850>.
- Bertels, L., Smets, B., Wolfs, D., 2016. Dynamic water surface detection algorithm applied on PROBA-V multispectral data. *Remote Sens.* 8:1010. <http://dx.doi.org/10.3390/rs8121010>.
- Boschetti, M., Nutini, F., Manfron, G., Brivio, P.A., Nelson, A., 2014. Comparative analysis of normalised difference spectral indices derived from MODIS for detecting surface water in flooded rice cropping systems. *PLoS One* 9, e88741. <http://dx.doi.org/10.1371/journal.pone.0088741>.
- Bureau of Reclamation of the U. S. Department of the Interior, 2016. *Reclamation-managing Water in the West [WWW Document]*. <http://www.usbr.gov/projects/dams.jsp>.
- Carroll, M.L., Townshend, J.R., DiMiceli, C.M., Noojipady, P., Sohlberg, R.A., 2009. A new global raster water mask at 250 m resolution. *Int. J. Digital Earth* 2:291–308. <http://dx.doi.org/10.1080/17538940902951401>.
- Cole, J.J., Prairie, Y.T., Caraco, N.F., McDowell, W.H., Tranvik, L.J., Striegl, R.G., Duarte, C.M., Kortelainen, P., Downing, J.A., Middelburg, J.J., Melack, J., 2007. Plumbing the global carbon cycle: integrating inland waters into the terrestrial carbon budget. *Ecosystems* 10:171–184. <http://dx.doi.org/10.1007/s10021-006-9013-8>.

- Congalton, R.G., Green, K., 2008. *Assessing the Accuracy of Remotely Sensed Data - Principles and Practices*. CRC Press, Boca Raton, FL.
- Copernicus GMES Initial Operations, 2013. *Gio Global Land Component - Lot I "Operation of the Global Land Component"* - ATBD 1–79.
- D'Andrimont, R., Pekel, J., Defourny, P., 2011. Monitoring African surface water dynamic using medium resolution daily data. *Proc. 2011 6th Int. Work. Anal. Multi-temporal Remote Sens. Images*:pp. 241–244 <http://dx.doi.org/10.1109/Multi-Temp.2011.6005093>.
- Dietz, A., Conrad, C., Kuenzer, C., Gesell, G., Dech, S., 2014. Identifying changing snow cover characteristics in Central Asia between 1986 and 2014 from remote sensing data. *Remote Sens.* 6:12752–12775. <http://dx.doi.org/10.3390/rs61212752>.
- Dodman, T., Diagona, C.H., 2006. Conservation dilemmas for intra-African migratory waterbirds. In: Boere, G.C., Galbraith, C.A., Stroud, D.A. (Eds.), *Waterbirds Around the World*. The Stationery Office Edinburgh, UK, pp. 218–223.
- Feng, L., Hu, C., Chen, X., Cai, X., Tian, L., Gan, W., 2012. Assessment of inundation changes of Poyang Lake using MODIS observations between 2000 and 2010. *Remote Sens. Environ.* 121:80–92. <http://dx.doi.org/10.1016/j.rse.2012.01.014>.
- Feng, L., Hu, C., Chen, X., Song, Q., 2014. Influence of the Three Gorges Dam on total suspended matters in the Yangtze Estuary and its adjacent coastal waters: observations from MODIS. *Remote Sens. Environ.* 140:779–788. <http://dx.doi.org/10.1016/j.rse.2013.10.002>.
- Feng, M., Sexton, J.O., Channan, S., Townshend, J.R., 2015. A global, high-resolution (30-m) inland water body dataset for 2000: first results of a topographic-spectral classification algorithm. *Int. J. Digital Earth* 8947:1–21. <http://dx.doi.org/10.1080/17538947.2015.1026420>.
- Feyisa, G.L., Meilby, H., Fensholt, R., Proud, S.R., 2014. Automated Water Extraction Index: a new technique for surface water mapping using Landsat imagery. *Remote Sens. Environ.* 140:23–35. <http://dx.doi.org/10.1016/j.rse.2013.08.029>.
- Fichtelmann, B., Borg, E., 2012. A new self-learning algorithm for dynamic classification of water bodies. In: Murgante, B., Gervasi, O., Misra, S., Nedjah, N., Rocha, A.M.A.C., Tanir, D., Apduhan, B.O. (Eds.), *Computational Science and Its Applications - ICCSA 2012, Part III*. Springer, Salvador de Bahia, Brazil, pp. 457–470.
- Fluet-Chouinard, E., Lehner, B., Rebelo, L.-M., Papa, F., Hamilton, S.K., 2014. Development of a global inundation map at high spatial resolution from topographic downscaling of coarse-scale remote sensing data. *Remote Sens. Environ.* 158:348–361. <http://dx.doi.org/10.1016/j.rse.2014.10.015>.
- Footy, G.M., 2006. What is the difference between two maps? A remote sensor's view. *J. Geogr. Syst.* 8:119–130. <http://dx.doi.org/10.1007/s10109-006-0023-z>.
- Friedl, M.A., Sulla-Menashe, D., Tan, B., Schneider, A., Ramankutty, N., Sibley, A., Huang, X., 2010. MODIS collection 5 global land cover: algorithm refinements and characterization of new datasets. *Remote Sens. Environ.* 114:168–182. <http://dx.doi.org/10.1016/j.rse.2009.08.016>.
- Gao, B., 1996. NDWI A Normalized Difference Water Index for Remote Sensing of Vegetation Liquid Water From Space. 266 pp. 257–266.
- Gardner, R.C., Barchiesi, S., Beltrame, C., Finlayson, C.M., Galewski, T., Harrison, I., Paganini, M., Perennou, C., Pritchard, D.E., Rosenqvist, A., Walpole, M., 2015. State of the world's wetlands and their services to people: a compilation of recent analyses. *Ramsar Brief. Note No. 7*:pp. 1–20 <http://dx.doi.org/10.2139/ssrn.2589447>.
- Gege, P., 2004. The water color simulator WASI: an integrating software tool for analysis and simulation of optical in situ spectra. *Comput. Geosci.* 30:523–532. <http://dx.doi.org/10.1016/j.cageo.2004.03.005>.
- Gessner, U., Machwitz, M., Esch, T., Tillack, A., Naeimi, V., Kuenzer, C., Dech, S., 2015. Multi-sensor mapping of West African land cover using MODIS, ASAR and Tandem-X/TerraSAR-X data. *Remote Sens. Environ.* 164:282–297. <http://dx.doi.org/10.1016/j.rse.2015.03.029>.
- Giardino, C., Bresciani, M., Villa, P., Martinelli, A., 2010. Application of remote sensing in water resource management: the case study of Lake Trasimeno, Italy. *Water Resour. Manag.* 24:3885–3899. <http://dx.doi.org/10.1007/s11269-010-9639-3>.
- Groove, T. De, Jr., Brakenridge, G.R., Flood, D., Adler, R., Ricko, M., Thielen, J., Jr., P.S., Policelli, F.S., Nasa, D.S., Albanese, A., Ithaca, E.C., Kuligowski, R., NOAA, S.K., 2013. Global Integrated Flood Map. <http://dx.doi.org/10.2788/8655>.
- Guerschman, J.P., Warren, G., Byrne, G., Lymburner, L., Mueller, N., Dijk, A. Van, 2011. MODIS-based standing water detection for flood and large reservoir mapping: algorithm development and applications for the Australian continent. *Www.Csro.Au* 88.
- Haas, E.M., Bartholomé, E., Combal, B., 2009. Time series analysis of optical remote sensing data for the mapping of temporary surface water bodies in sub-Saharan western Africa. *J. Hydrol.* 370:52–63. <http://dx.doi.org/10.1016/j.jhydrol.2009.02.052>.
- Hall, D.K., Riggs, G.A., 2007. Accuracy Assessment of the MODIS Snow Products. 1547: pp. 1534–1547. <http://dx.doi.org/10.1002/hyp>.
- Hein, L., 2006. The impacts of grazing and rainfall variability on the dynamics of a Sahelian rangeland. *J. Arid Environ.* 64:488–504. <http://dx.doi.org/10.1016/j.jaridenv.2005.06.014>.
- Jain, S.K., Singh, R.D., Jain, M.K., Lohani, A.K., 2005. Delineation of flood-prone areas using remote sensing techniques. *Water Resour. Manag.* 19:333–347. <http://dx.doi.org/10.1007/s11269-005-3281-5>.
- Jain, S.K., Saraf, A.K., Goswami, A., Ahmad, T., 2006. Flood inundation mapping using NOAA AVHRR data. *Water Resour. Manag.* 20:949–959. <http://dx.doi.org/10.1007/s11269-006-9016-4>.
- Jarvis, A., Reuter, H.I., Nelson, A., Guevara, E., 2008. *Hole-filled Seamless SRTM Data V4*. International Centre for Tropical Agriculture (CIAT).
- Ji, L., Zhang, L., Wylie, B., 2009. Analysis of Dynamic Thresholds for the Normalized Difference Water Index. 75 pp. 1307–1317.
- Klein, I., Dietz, A.J., Gessner, U., Galayeva, A., Myrzhakmetov, A., Kuenzer, C., 2014. Evaluation of seasonal water body extents in Central Asia over the past 27 years derived from medium-resolution remote sensing data. *Int. J. Appl. Earth Obs. Geoinf.* 26: 335–349. <http://dx.doi.org/10.1016/j.jag.2013.08.004>.
- Klein, I., Dietz, A., Gessner, U., Dech, S., Kuenzer, C., 2015. Results of the Global WaterPack: a novel product to assess inland water body dynamics on a daily basis. *Remote Sens. Lett.* 6:78–87. <http://dx.doi.org/10.1080/2150704X.2014.1002945>.
- Klotz, M., Kemper, T., Geiß, C., Esch, T., Taubenböck, H., 2016. How good is the map? A multi-scale cross-comparison framework for global settlement layers: Evidence from Central Europe. *Remote Sens. Environ.* 178:191–212. <http://dx.doi.org/10.1016/j.rse.2016.03.001>.
- Kuenzer, C., Guo, H., Huth, J., Leinenkugel, P., Li, X., Dech, S., 2013. Flood mapping and flood dynamics of the Mekong Delta: ENVISAT-ASAR-WSM based time series analyses. *Remote Sens.* 5:687–715. <http://dx.doi.org/10.3390/rs5020687>.
- Kuenzer, C., Klein, I., Ullmann, T., Georgiou, E.F., Baumhauer, R., Dech, S., 2015. Remote sensing of river delta inundation: exploiting the potential of coarse spatial resolution, temporally-dense MODIS time series. *Remote Sens.* 7:8516–8542. <http://dx.doi.org/10.3390/rs70708516>.
- Land Processes Distributed Active Archive Center, 2015. URL. <https://lpdaac.usgs.gov/> [WWW Document].
- Lehner, B., Döll, P., 2004. Development and validation of a global database of lakes, reservoirs and wetlands. *J. Hydrol.* 296:1–22. <http://dx.doi.org/10.1016/j.jhydrol.2004.03.028>.
- Li, S., Sun, D., Goldberg, M., Stefanidis, A., 2013. Derivation of 30-m-resolution water maps from TERRA/MODIS and SRTM. *Remote Sens. Environ.* 134:417–430. <http://dx.doi.org/10.1016/j.rse.2013.03.015>.
- Liu, Y., 2012. Why NDWI threshold varies in delineating water body from multitemporal images? *Int. Geosci. Remote Sens. Symp.*:pp. 4375–4378 <http://dx.doi.org/10.1109/IGARSS.2012.6350404>.
- Mack, B., Leinenkugel, P., Kuenzer, C., Dech, S., 2017. A semi-automated approach for the generation of a new land use and land cover product for Germany based on Landsat time-series and Lucas in-situ data. *Remote Sens. Lett.* 8:244–253. <http://dx.doi.org/10.1080/2150704X.2016.1249299>.
- Martinis, S., Twele, A., Strobl, C., Kersten, J., Stein, E., 2013. A multi-scale flood monitoring system based on fully automatic MODIS and TerraSAR-X processing chains. *Remote Sens.* 5:5598–5619. <http://dx.doi.org/10.3390/rs5115598>.
- Martinis, S., Kuenzer, C., Wendleder, A., Huth, J., Twele, A., Roth, A., Dech, S., 2015. Comparing four operational SAR-based water and flood detection approaches. *Int. J. Remote Sens.* 36:3519–3543. <http://dx.doi.org/10.1080/01431161.2015.1060647>.
- Mason, I.M., Gzuskowska, M., Rapley, C.G., Street-Perrott, F.A., 1994. The response of lake levels and are as to climatic change. *Clim. Chang.* 27, 161–197.
- McCullough, I.M., Loftin, C.S., Sader, S.A., 2012. High-frequency remote monitoring of large lakes with MODIS 500m imagery. *Remote Sens. Environ.* 124:234–241. <http://dx.doi.org/10.1016/j.rse.2012.05.018>.
- McFEETERS, S.K., 1996. The use of the Normalized Difference Water Index (NDWI) in the delineation of open water features. *Int. J. Remote Sens.* 17:1425–1432. <http://dx.doi.org/10.1080/01431169608948714>.
- Mueller, N., Lewis, A., Roberts, D., Ring, S., Melrose, R., Sixsmith, J., Lymburner, L., McIntyre, A., Tan, P., Curnow, S., Ip, A., 2016. Remote Sensing of Environment Water Observations From Space: Mapping Surface Water From 25 Years of Landsat Imagery Across Australia. 174:pp. 341–352. <http://dx.doi.org/10.1016/j.rse.2015.11.003>.
- Nigro, J., Slayback, D., Policelli, F., Brakenridge, G.R., 2014. NASA/DFO MODIS Near Real-Time (NRT) Global Flood Mapping Product Evaluation of Flood and Permanent Water Detection. pp. 1–27.
- Ogilvie, A., Belaud, G., Delenne, C., Bailly, J.-S., Bader, J.-C., Oleksiak, A., Ferry, L., Martin, D., 2015. Decadal monitoring of the Niger Inner Delta flood dynamics using MODIS optical data. *J. Hydrol.* 523:368–383. <http://dx.doi.org/10.1016/j.jhydrol.2015.01.036>.
- Olson, D.M., Dinerstein, E., E.E.D.W.K., Burgess, N.D., L.G.V.N.P.O.W.E.L., D.E.C.U.O., Amico, J.A.D., Itoua, I., Strand, H.O.L.L.Y.E., Morrison, J.C., 2001. *Terrestrial Ecoregions of the World: A New Map of Life on Earth*. 51 pp. 933–938.
- Palmer, S.C.J., Kutser, T., Hunter, P.D., 2015. Remote sensing of inland waters: challenges, progress and future directions. *Remote Sens. Environ.* 157:1–8. <http://dx.doi.org/10.1016/j.rse.2014.09.021>.
- Papa, F., Prigent, C., Aires, F., Jimenez, C., Rossow, W.B., Matthews, E., 2010. Interannual variability of surface water extent at the global scale, 1993–2004. *J. Geophys. Res. Atmos.* 115:1–17. <http://dx.doi.org/10.1029/2009JD012674>.
- Pekel, J.-F., Vancutsem, C., Bastin, L., Clerici, M., Vanbogaert, E., Bartholomé, E., Defourny, P., 2014. A near real-time water surface detection method based on HSV transformation of MODIS multi-spectral time series data. *Remote Sens. Environ.* 140:704–716. <http://dx.doi.org/10.1016/j.rse.2013.10.008>.
- Pekel, J.-F., Cottam, A., Gorelick, N., Belward, A.S., 2016. High-resolution mapping of global surface water and its long-term changes. *Nature*:1–19 <http://dx.doi.org/10.1038/nature20584>.
- Richter, R., Schlaffer, D., 2007. Atmospheric/topographic Correction for Satellite Imagery (ATCOR-2/3 User Guide). ATCOR-2/3 User Guide. Version 6.3. <http://dx.doi.org/10.1017/CBO9781107415324.004>.
- Riggs, G.A., Hall, D.K., Salomonson, V.V., 2006. *MODIS Snow Products User Guide to Collection. p. 5*.
- Schoene, T., Dusik, E., Illigner, J., Klein, I., 2016. Water in Central Asia - reservoir level monitoring with radar altimetry. *Int. Assoc. Geod. Symp.* pp. 1–9.
- Sheng, Y., Song, C., Wang, J., Lyons, E.A., Knox, B.R., Cox, J.S., Gao, F., 2016. Representative lake water extent mapping at continental scales using multi-temporal Landsat-8 imagery. *Remote Sens. Environ.* 185:129–141. <http://dx.doi.org/10.1016/j.rse.2015.12.041>.
- Slater, J.A., Garvey, G., Johnston, C., Haase, J., Heady, B., Kroenung, G., Little, J., 2006. The SRTM data finishing process and products. *Photogramm. Eng. Remote. Sens.* 72 (3), 237–247.
- Sun, D., Yu, Y., Goldberg, M.D., 2011. Deriving water fraction and flood maps from MODIS images using a decision tree approach. *IEEE J. Sel. Top. Appl. Earth Obs. Remote Sens.* 4:814–825. <http://dx.doi.org/10.1109/JSTARS.2011.2125778>.

- Sun, F., Sun, W., Chen, J., Gong, P., 2012. Comparison and improvement of methods for identifying waterbodies in remotely sensed imagery. *Int. J. Remote Sens.* 33: 6854–6875. <http://dx.doi.org/10.1080/01431161.2012.692829>.
- Ticehurst, C., Guerschman, J., Yun, C., 2014. The strengths and limitations in using the daily MODIS open water likelihood algorithm for identifying flood events. *Remote Sens.* 6:11791–11809. <http://dx.doi.org/10.3390/rs61211791>.
- Tulbure, M.G., Broich, M., Stehman, S.V., Kommareddy, A., 2016. Surface water extent dynamics from three decades of seasonally continuous Landsat time series at subcontinental scale in a semi-arid region. *Remote Sens. Environ.* 178:142–157. <http://dx.doi.org/10.1016/j.rse.2016.02.034>.
- Vermote, E.F., Kotchenova, S.Y., Ray, J.P., 2011. *MODIS Surface Reflectance User's Guide*. pp. 1–40.
- Verpoorter, C., Kutser, T., Seekell, D.A., Tranvik, L.J., 2014. A Global Inventory of Lakes Based on High-resolution Satellite Imagery. :pp. 1–7 <http://dx.doi.org/10.1002/2014GL060641>. Received.
- WMO, 2016. *The Global Observing System for Climate: Implementation Needs*. 200 p. 325.
- Xu, H., 2006. Modification of normalised difference water index (NDWI) to enhance open water features in remotely sensed imagery. *Int. J. Remote Sens.* 27:3025–3033. <http://dx.doi.org/10.1080/01431160600589179>.
- Yamazaki, D., Trigg, M.A., 2016. Hydrology: the dynamics of Earth's surface water. *Nature* <http://dx.doi.org/10.1038/nature21100>.
- Yamazaki, D., Trigg, M.A., Ikeshima, D., 2015. Development of a global ~90 m water body map using multi-temporal Landsat images. *Remote Sens. Environ.* 171:337–351. <http://dx.doi.org/10.1016/j.rse.2015.10.014>.
- Zedler, P.H., 2003. Vernal pools and the concept of “isolated wetlands”. *Wetlands* 23: 597–607. [http://dx.doi.org/10.1672/0277-5212\(2003\)023\[0597:VPATCO\]2.0.CO;2](http://dx.doi.org/10.1672/0277-5212(2003)023[0597:VPATCO]2.0.CO;2).
- Zhu, Z., Wang, S., Woodcock, C.E., 2015. Improvement and expansion of the Fmask algorithm: cloud, cloud shadow, and snow detection for Landsats 4–7, 8, and Sentinel 2 images. *Remote Sens. Environ.* 159:269–277. <http://dx.doi.org/10.1016/j.rse.2014.12.014>.